CMS Physics Analysis Summary

Search for light pseudoscalar bosons produced in Higgs boson decays in the 4τ and $2\mu2\tau$ final states in proton-proton collisions at $\sqrt{s} = 13$ TeV

The CMS Collaboration

Abstract

A search for a pair of light pseudoscalar bosons (a_1) produced from the decay of the 125 GeV Higgs boson (H) is presented. The analysis examines decay modes where one a_1 decays into a pair of tau leptons, and the other decays into either another pair of tau leptons or a pair of muons. The a_1 mass probed in this study ranges from 4 to 15 GeV. The data sample used was recorded by the CMS experiment in proton-proton collisions at a center-of-mass energy of 13 TeV and corresponds to an integrated luminosity of 138 fb^{-1}. The study uses the $2\mu2\tau$ and 4τ channels in combination to constrain the product of the Higgs boson production cross section and the branching fraction to the 4τ final state, $\sigma(pp \to H + X)\mathcal{B}(H \to a_1a_1)\mathcal{B}^2(a_1 \to \tau\tau)$. This methodology takes advantage of the linear dependence of the fermionic coupling strength of pseudoscalar bosons on the fermion mass. Model-independent upper limits at 95% confidence level (CL) on $\sigma(pp \to H + X)\mathcal{B}(H \to a_1a_1)\mathcal{B}^2(a_1 \to \tau\tau)$, relative to the standard model Higgs boson production cross section σ_{SM}, are set. The observed (expected) upper limits range between 0.007 (0.011) and 0.079 (0.066) across the mass range considered. Exclusion limits at 95% on $\sigma(pp \to H + X)\mathcal{B}(H \to a_1a_1)$, relative to σ_{SM}, are derived for various Two Higgs Doublet Model + Singlet scenarios.

1 Introduction

The discovery of the Higgs boson (H) with a mass of 125 GeV [1–3] by the ATLAS and CMS Collaborations at the CERN LHC reconfirmed the standard model (SM) as the most robust framework to date describing the fundamental particles and their interactions in the universe. However, it is well recognized that the SM is not a complete theory. It does not adequately explain key phenomena, such as the nature of dark matter, the origin of neutrino masses, and the matter-antimatter asymmetry in the universe. Consequently, numerous extensions to the SM have been proposed, which include the 125 GeV Higgs boson as part of their frameworks while also addressing some of the shortcomings of the SM. Examples of such extensions are the Minimal Supersymmetric Standard Model (MSSM) [4, 5], the Next-to-Minimal Supersymmetric Standard Model (NMSSM) [6, 7], the Two-Higgs-Doublet Model (2HDM) [8, 9], 2HDM with an additional complex scalar singlet field (2HDM+S) [10] and the Little Higgs Model (LHM) [11, 12].

Among these extended models, the 2HDM+S model is particularly interesting. The inclusion of the singlet provides a natural candidate for dark matter through the presence of stable particles [13]. The model also offers a solution to the matter-antimatter asymmetry by introducing new sources of CP violation [14]. Furthermore, the NMSSM can be viewed as a special case of 2HDM+S, where the inclusion of the singlet field helps address the so-called μ-problem [15, 16]. The 2HDM+S predicts seven physical Higgs boson states: three CP-even, two CP-odd, and two charged bosons. One of the scalars can be identified as the discovered Higgs boson with a mass of 125 GeV. At the same time, one of the two pseudoscalars, denoted a_1, can be light enough for the $H \to a_1 a_1$ decays to be kinematically possible. Measurements of the Higgs couplings so far permit a substantial branching fraction for Higgs decays to beyond-the-SM (BSM) particles, with the ATLAS and CMS experiments having established upper limits at 95% confidence level (CL) of 12 and 16%, respectively [17, 18]. This renders the investigation of the $H \to a_1 a_1$ decays an effective probe of potential extensions to the SM and the discovery of new physics phenomena.

Models with two Higgs doublets and one singlet predict various decay channels for the pseudoscalar boson a_1, with significant branching ratios into fermion pairs. The decay patterns of a_1 are governed by parameters, such as the ratio $\tan\beta$ of the vacuum expectation values of the two Higgs doublets and the mass, m_{a_1}, of the a_1 boson. The different variants of 2HDM+S – Type I, II, III, and IV – differ in how the Higgs doublets, Φ_1 and Φ_2, couple to fermions, resulting in distinct decays. In Type I models, where all fermions couple only to Φ_2, the $a_1 \to c\bar{c}$ decay dominates for $2m_c < m_{a_1} < 2m_b$, where m_c and m_b are the masses of the c- and b-quarks, respectively. For $m_{a_1} > 2m_b$, $a_1 \to b\bar{b}$ becomes the leading decay mode. In Type IV models, leptons and up-type quarks couple to Φ_2, while down-type quarks couple to Φ_1, often enhancing decays to down-type quarks at high $\tan\beta$. In Type II models, up-type quarks couple to Φ_2, while down-type quarks and leptons couple to Φ_1. Enhanced couplings to down-type quarks and leptons, proportional to $\tan\beta$, make the $a_1 \to \tau\tau$ decay dominant for $2m_\tau < m_{a_1} < 2m_b$, where m_τ is the mass of τ lepton. For $\tan\beta > 1$, the branching ratio often exceeds 90%. As the mass increases, $a_1 \to b\bar{b}$ becomes significant. However, in certain 2HDM+S models, the $a_1 \to \tau\tau$ can still dominate above the $a_1 \to b\bar{b}$ threshold. This is realized at $\tan\beta > 1$ in Type III models, where leptons couple to Φ_1, and Φ_2 couples to up- and down-type quarks. Given the potential dominance of $a_1 \to \tau\tau$ in several 2HDM+S scenarios, this channel offers a promising search avenue.

Several searches for $H \to a_1 a_1$ decays have been carried out by the ATLAS and CMS Collaborations to date, exploring different decay modes of a_1, covering the mass range $0.2 < m_{a_1} <$

62.5 GeV [19–36]. The studies did not reveal significant deviations from the SM background expectations, and upper limits were set on the signal rates, thereby constraining the parameters of the 2HDM+S.

In this note, a search for light a_1 via the $H \to a_1 a_1 \to 4\tau$ and $H \to a_1 a_1 \to 2\mu 2\tau$ decay modes is presented. The analysis is based on proton-proton (pp) collision data at a center-of-mass energy of 13 TeV, corresponding to an integrated luminosity of 138 fb^{-1}, recorded by the CMS detector in 2016–2018. The analysis covers a_1 masses from 4 to 15 GeV and employs a specialized analysis strategy to select and identify highly Lorentz-boosted muon or tau lepton pairs with overlapping decay products. A similar search was carried out by CMS previously based on a data sample of 35.9 fb^{-1} at $\sqrt{s}$ = 13 TeV, setting observed upper limits at 95% CL on the product of the H production cross section and the branching fraction of the $H \to a_1 a_1 \to 4\tau$ decay, relative to the inclusive cross section of the SM Higgs production, between 0.022 and 0.23 [33]. The current study extends the previous analysis by utilizing a data set approximately four times larger and optimizing the event selection criteria, thus bringing about higher sensitivity to potential signals.

The signal topology targeted by the present analysis is illustrated in Fig. 1, where the Higgs boson decays into a pair of a_1 bosons. Each a_1 boson is identified by the presence of a muon and a close-by additional charged particle, which could be an electron, muon, or charged hadron ($e^{\pm}/\mu^{\pm}/h^{\pm}$). These charged particles are characterized by the presence of one reconstructed track with a charge opposite to that of the muon. The analysis focuses on the $a_1 a_1 \to (\tau_\mu \tau_{\text{1-prong}})(\tau_\mu \tau_{\text{1-prong}})$ decays, where the τ_μ denotes the muonic decay of the tau lepton and $\tau_{\text{1-prong}}$ stands for its leptonic or 1-prong hadronic decays. The 3-prong tau decays are excluded due to their very high multijet background and lower reconstruction efficiency. Although the analysis primarily targets the $(\tau_\mu \tau_{\text{1-prong}})(\tau_\mu \tau_{\text{1-prong}})$ decays, $a_1 a_1 \to (\mu\mu)(\tau_\mu \tau_{\text{1-prong}})$ are also included as they give rise to the same topology.

Given the significant mass difference between a_1 and H bosons, the a_1 bosons are produced with a high Lorentz boost, leading to collimated decay products. The analysis primarily focuses on the dominant gluon-gluon fusion (ggF) production mechanism, where the H boson is produced with relatively small transverse momentum (p_T) and the a_1 pseudoscalars are emitted nearly back-to-back in the transverse plane, resulting in a large separation in azimuthal angle ($\Delta\phi$) between the decay products of the two a_1. When the H boson is produced with high transverse momentum, e.g., due to initial state radiation in ggF, or through other production mechanisms, the azimuthal angle between the a_1 bosons is reduced, while the separation in pseudorapidity η can still be large. The analysis focuses on identification of same-charge (SC) dimuon events with significant angular separation, $\Delta R = \sqrt{(\Delta\phi)^2 + (\Delta\eta)^2}$, where each muon is accompanied by a nearby oppositely charged particle from the same a_1 decay. The requirement of same-charge muons significantly reduces backgrounds from top quark pairs, Drell–Yan processes, and diboson production, enhancing the sensitivity of the search.

2 The CMS detector

The central feature of the CMS apparatus is a superconducting solenoid of 6 m internal diameter, providing a magnetic field of 3.8 T. Within the solenoid volume are a silicon pixel and strip tracker, a lead tungstate crystal electromagnetic calorimeter (ECAL), and a brass and scintillator hadron calorimeter (HCAL), each composed of a barrel and two endcap sections. Forward calorimeters extend the pseudorapidity coverage provided by the barrel and endcap detectors. Muons are reconstructed in gas-ionization detectors embedded in the steel flux-return
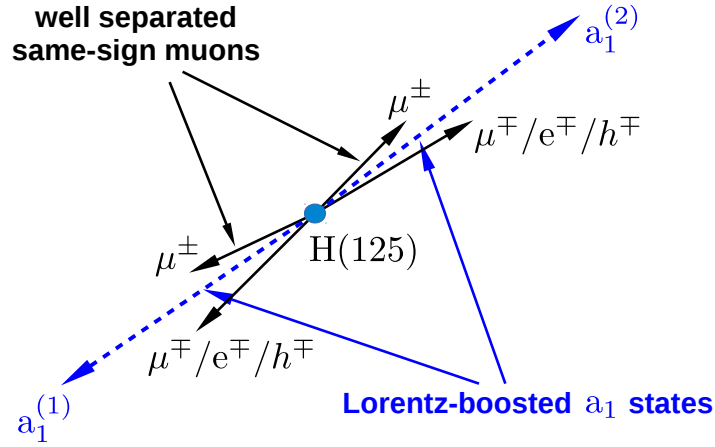
Figure 1: Illustration of the signal topology, in which the H boson decays into two a_1 bosons, where one a_1 boson decays into a pair of tau leptons, while the other decays into a pair of muons or a pair of tau leptons. The analyzed final state consists of one muon and an oppositely charged track in each a_1 decay.

yoke outside the solenoid. More detailed descriptions of the CMS detector, together with a definition of the coordinate system used and the relevant kinematic variables, can be found in Refs. [37, 38].

Events of interest are selected using a two-tiered trigger system. The first level (L1), composed of custom hardware processors, uses information from the calorimeters and muon detectors to select events at a rate of around 100 kHz within a fixed latency of 4 μs [39]. The second level, known as the high-level trigger (HLT), consists of a farm of processors running a version of the full event reconstruction software optimized for fast processing, which reduces the event rate to around 1 kHz before data storage [40].

3 Simulated samples

Signal events in the H $\rightarrow a_1a_1 \rightarrow 4\tau$ channel are simulated at leading order (LO) in perturbative QCD using the PYTHIA (v.8.212) event generator [41], targeting four major Higgs production mechanisms: gluon-gluon fusion; vector boson fusion (VBF); Higgs-strahlung (VH); and top quark pair associated production (t$\bar{\text{t}}$H). For the H $\rightarrow a_1a_1 \rightarrow 2\mu2\tau$ decay channel, events are generated at LO for the dominant ggF production mode using MADGRAPH5_aMC@NLO (v.2.6.5) [42]. The p_T distribution of the Higgs boson produced via ggF is reweighted for both decay channels (4τ and $2\mu2\tau$) using next-to-next-to-leading order (NNLO) k-factors computed with the program HQT (v.2.0) [43, 44], taking into account the NNLO NNPDF3.1 parton distribution functions (PDF) [45]. For VBF and VH processes, the p_T distribution of the H bosons is reweighted using k-factors calculated with the next-to-leading order (NLO) POWHEGBOX (v.2.0) event generator [46–48]. In the case of t$\bar{\text{t}}$H production, the NLO k-factors are determined using MADGRAPH5_aMC@NLO.

The major source of background for the analysis is the QCD production of multijets, followed by smaller contributions from Drell–Yan processes with a Z boson or from W boson production, accompanied by jets (Z+jets and W+jets), production of a top quark-antiquark pair with addi-

tional jets (t$\bar{\text{t}}$+jets), single top quark production, and vector boson pair production (diboson). The QCD multijet and diboson backgrounds are simulated using PYTHIA, whereas the Z+jets and W+jets backgrounds are generated at LO with MADGRAPH5_aMC@NLO. The single-top and t$\bar{\text{t}}$+jets processes are generated at NLO using POWHEGBOX.

Parton showering and fragmentation for all Monte Carlo (MC) samples are executed using PYTHIA (v.8.212). The CP5 tune is applied to describe the underlying events [49]. The simulations utilize the NNPDF3.1 PDFs [45]. For samples produced with MADGRAPH5_aMC@NLO, the MLM matching scheme [50] is employed for LO samples. The detector response is simulated with the GEANT4 package [51, 52]. The contribution of additional proton-proton collisions within the same or proximate bunch crossings (referred to as pileup) is replicated through the simulation of minimum bias interactions, which are then superimposed onto the primary hard-scattering events. The simulated events are then reweighted to reflect the observed pileup distribution in the experimental data.

4 Event reconstruction

The analysis selects events containing two muons and two additional tracks in the final state, and thus, an accurate reconstruction of these objects is crucial. The event reconstruction involves several steps, including track reconstruction, primary vertex (PV) identification, the application of the Particle Flow (PF) algorithm [53], and detailed muon reconstruction to achieve high precision in particle identification.

Track reconstruction is primarily performed using the Combinatorial Track Finder (CTF) algorithm, which employs Kalman filtering to refine track estimates [54]. The tracks are reconstructed from hits in the CMS tracker and are evaluated based on several quality criteria: fit quality, assessed by the chi-squared per degree of freedom (χ^2/ndf) of the track fit; the number of hits associated with the track, with higher counts indicating better quality; the distance of closest approach of the track to the primary vertex, both in the transverse plane ($|d_0|$) and along the z-axis ($|d_z|$); and the pattern of hits across different tracker layers. The analysis uses the so-called high-purity tracks that meet stringent quality criteria [54]. These tracks typically have a high number of hits, a low χ^2/ndf, and a small impact parameter relative to the PV.

The PV is identified as the vertex corresponding to the hardest scattering in the event, evaluated using tracking information alone, as described in Section 9.4.1 of Ref. [55].

The PF algorithm is used to reconstruct and identify each particle in an event (PF candidate) with an optimized combination of all subdetector information. The PF algorithm identifies photons originating from, e.g., π^0 decays or from electron bremsstrahlung, as ECAL energy clusters not linked to the extrapolation of any charged particle trajectory to the ECAL. Electrons arising from, e.g., photon conversions in the tracker material or from semileptonic decays of heavy-flavor hadrons are identified as primary charged particle tracks associated with multiple ECAL energy clusters corresponding to the track's extrapolation to the ECAL and possible bremsstrahlung photons emitted through the tracker material. Muons, e.g., produced in semileptonic heavy hadron decays, are identified as tracks in the central tracker consistent with either a track or several hits in the muon system and associated with calorimeter deposits compatible with the muon hypothesis. Charged hadrons are identified as charged particle tracks, neither identified as electrons nor as muons. Finally, neutral hadrons are identified as HCAL energy clusters not linked to any charged hadron trajectory or as a combined ECAL and HCAL energy excess with respect to the expected charged hadron energy deposit.

To suppress contributions from nonprompt decays of hadrons into muons and their punch-through to the muon detectors, the PF muons are further required to pass dedicated identification requirements, which depend on several parameters, including track quality, impact parameter significance, and muon chamber hits. The analysis employs the medium identification criteria [56], which yield an overall efficiency between 98 and 99% for muons with $p_T > 20\,\text{GeV}$ in data. Scale factors, derived by comparing the muon identification efficiencies between data and MC, are applied to the simulation to better match the muon performance observed in data.

For each event, jets are reconstructed by clustering PF candidates using the anti-k_T algorithm [57, 58] with a distance parameter of 0.4. Charged particles not associated with the PV are excluded from the clustering using the charged hadron subtraction (CHS) method [53]. The reconstructed jet energies are corrected in both data and simulation to account for effects from the nonlinear detector response and contamination from pileup [59]. The resolution of the jet energy is also corrected in simulation to improve the agreement with data. Jets are primarily used in the analysis to identify and veto jets containing bottom quarks (b jets).

The b jets are identified by applying the DEEPJET algorithm [60, 61] to the selected jets. The tight working point of the b tagging discriminator, which corresponds to a rate of 0.1% for misidentifying a light jet (i.e., gluons and light-quark jets) as a b jet, is used [62]. The corresponding b tagging efficiency, measured in $t\bar{t}$+jets events, is around 65%. Small differences between data and simulation for b tagging efficiencies are corrected. QCD multijet events with heavy hadrons that decay muonically via semileptonic decay form a significant background for the analysis. Hence, a veto of b jets is essential for reducing this background.

5 Event selection

Events of interest are recorded using a set of dimuon triggers. For the 2016 and 2017 data, the triggers required the leading (subleading) muon to have a p_T of at least 17 (8) GeV. The p_T thresholds in 2018 were raised to 18 and 9 GeV for the leading and subleading muon, respectively. Additionally, in 2016 and 2018, the triggers required the two muons to have the same charge. In 2016, it was also required that the tracks of the two muons have their points of closest approach to the beam axis within 2 mm of each other along the longitudinal direction. Due to technical limitations, the trigger imposing the same-charge criterion was not available for the entire 2017 data-taking period. An alternate trigger imposing a loose muon isolation criterion was used instead. This criterion required the ratio of the p_T-sum of charged hadrons within an isolation cone of size $\Delta R = 0.3$ around the muon to the p_T of the muon to be less than 0.4. Despite this requirement, it was found that this trigger was still efficient in selecting nonisolated muons with high efficiency, thereby demonstrating good acceptance for selecting events compatible with the signal topology of this search.

In the offline selection, as the first step, a b jet veto is imposed by rejecting events containing one or more b tagged jets with $p_T > 20\,\text{GeV}$ and $|\eta| < 2.4$. Following the veto, the remaining events that pass the trigger selection criteria are required to contain at least two SC muons. The muons must lie within $|\eta| < 2.4$. The p_T of the leading muon is required to be greater than 19 GeV, and that of the subleading muon to be greater than 10 GeV. The transverse (longitudinal) impact parameters of the muons with respect to the primary vertex are required to be $|d_0| < 0.05$ ($|d_z| < 0.1$) cm. The angular separation between the muons must be $\Delta R > 1.5$. If more than one pair of SC muons meets these criteria, the pair with the highest scalar sum of p_T is selected.

The next step of the selection employs information of tracks associated with the reconstructed charged PF objects, excluding the pair of SC muons, to identify and isolate the candidates for

the $a_1 \to \tau_\mu \tau_{1\text{-prong}}$ or $a_1 \to \mu\mu$ decays, hereafter referred to as a_1 candidates. Two types of tracks are considered, namely "isolation" and "signal" tracks. The "signal" tracks are a subset of the "isolation" tracks, subject to stricter selection criteria. The specific selection criteria and usage of these tracks are detailed in Table 1.

Table 1: Types of tracks considered in the analysis, with their selection criteria and purposes.

Type of track	p_T	$|\eta|$	$|d_0|$ w.r.t. PV	$|d_z|$ w.r.t. PV	Purpose
Isolation	$> 1.0\,\text{GeV}$	< 2.4	$< 0.2\,\text{cm}$	$< 0.3\,\text{cm}$	Define isolation criterion for the a_1 candidates
Signal	$> 2.5\,\text{GeV}$	< 2.4	$< 0.02\,\text{cm}$	$< 0.04\,\text{cm}$	Build a_1 candidates

Each selected muon of the SC pair is required to have exactly one "isolation" track within a ΔR cone of 0.5 around the muon. The background components, especially QCD multijet events, tend to have higher track multiplicity with respect to the signal and, hence, are rejected by imposing such an isolation requirement. A muon-track system is accepted as an a_1 candidate if the isolation track around each muon meets the signal track criteria. The event is selected in the final sample if it contains two a_1 candidates. The set of selection requirements outlined above defines the signal region (SR).

The number of observed events selected in the SR is 7803. A simulation study indicates that QCD multijet events are the predominant background in the SR. Contributions from other background sources are minimal, comprising about 1% of events selected in the SR. The expected signal acceptance and signal yield for a few representative values of m_{a_1} are reported in Table 2. The acceptance is evaluated relative to the total H boson production cross section, assuming the SM predictions for the various production modes — 48.58 pb for ggF, 3.78 pb for VBF, 2.26 pb for VH, and 0.51 pb for ttH [63]. The signal yields are calculated assuming a benchmark value of the branching fraction, $\mathcal{B}(\text{H} \to a_1 a_1)\mathcal{B}^2(a_1 \to \tau\tau) = 0.05$, and the SM H production cross sections. Contributions from the ggF, VBF, VH, and $t\bar{t}$H processes are summed up to determine the 4τ yield. The yield of the $2\mu2\tau$ signal is estimated under the assumption that the partial widths of the $a_1 \to \mu\mu$ and $a_1 \to \tau\tau$ decays satisfy the relation [64]

$$\frac{\Gamma(a_1 \to \mu\mu)}{\Gamma(a_1 \to \tau\tau)} = \frac{m_\mu^2}{m_\tau^2 \sqrt{1 - \left(2m_\tau/m_{a_1}\right)^2}}. \tag{1}$$

Using this relation between the partial widths, the ratio of branching fractions for $a_1 a_1 \to 2\mu2\tau$ and $a_1 a_1 \to 4\tau$ decays is computed as

$$\frac{\mathcal{B}(a_1 a_1 \to 2\mu2\tau)}{\mathcal{B}(a_1 a_1 \to 4\tau)} = 2\frac{\mathcal{B}(a_1 \to \mu\mu)}{\mathcal{B}(a_1 \to \tau\tau)} = 2\frac{\Gamma(a_1 \to \mu\mu)}{\Gamma(a_1 \to \tau\tau)}. \tag{2}$$

The factor of 2 in Eq. (2) accounts for the two possible decay combinations: $a_1^{(1)} a_1^{(2)} \to 2\mu2\tau$ and $a_1^{(1)} a_1^{(2)} \to 2\tau2\mu$, both producing a final state with two muons and two tau leptons. The ratio in Eq. (2) varies from about 0.0073 at $m_{a_1} = 15\,\text{GeV}$ to 0.0155 at $m_{a_1} = 4\,\text{GeV}$. To account for contributions from production modes other than ggF to the $2\mu2\tau$ final state, the analysis assumes identical acceptance ratios between $2\mu2\tau$ and 4τ channels across the different production mechanisms, scaling the ggF acceptance accordingly to estimate the total $2\mu2\tau$ yield.

Table 2: The signal acceptance and the number of expected signal events after selection in the SR. The acceptance is calculated relative to the total H production cross section, using values predicted by the SM. The number of expected signal events is computed for a benchmark value of the branching fraction $\mathcal{B}(H \rightarrow a_1 a_1)\mathcal{B}^2(a_1 \rightarrow \tau\tau) = 0.05$, assuming SM-predicted cross sections. The quoted uncertainties for the predictions from simulation include only statistical uncertainties.

m_{a_1} [GeV]	Acceptance $\times 10^4$		Number of events	
	4τ	$2\mu2\tau$	4τ	$2\mu2\tau$
5	3.52 ± 0.10	103.21 ± 1.17	133.9 ± 3.8	39.7 ± 0.4
8	2.55 ± 0.09	76.00 ± 0.98	97.2 ± 3.3	23.0 ± 0.3
12	1.37 ± 0.06	35.58 ± 0.66	52.1 ± 2.4	10.1 ± 0.2
15	0.32 ± 0.03	7.53 ± 0.33	12.3 ± 1.1	2.1 ± 0.1

The two-dimensional (2D) distribution of the invariant masses of the muon-track systems, which constitute the a_1 candidates, is employed to distinguish between the signal and the background in the signal extraction procedure. This 2D distribution is populated with pairs of muon-track invariant masses (m_1, m_2), ordered by their value, $m_2 > m_1$. The binning of the 2D distribution used in the analysis is illustrated in Fig. 2. Since m_2 is required to be greater than m_1, only the bins (i, j) where $j \geq i$ are filled, resulting in a total of $6(6+1)/2 = 21$ independent bins. The bin boundaries along each axis are $(0.0, 1.0, 2.0, 3.0, 4.0, 5.2)$. Bins $(i, 6)$ with $i = 1$-5 include all events with $m_2 > 5.2\,\text{GeV}$, while bin $(6, 6)$ contains all events with $m_{1,2} > 5.2\,\text{GeV}$.
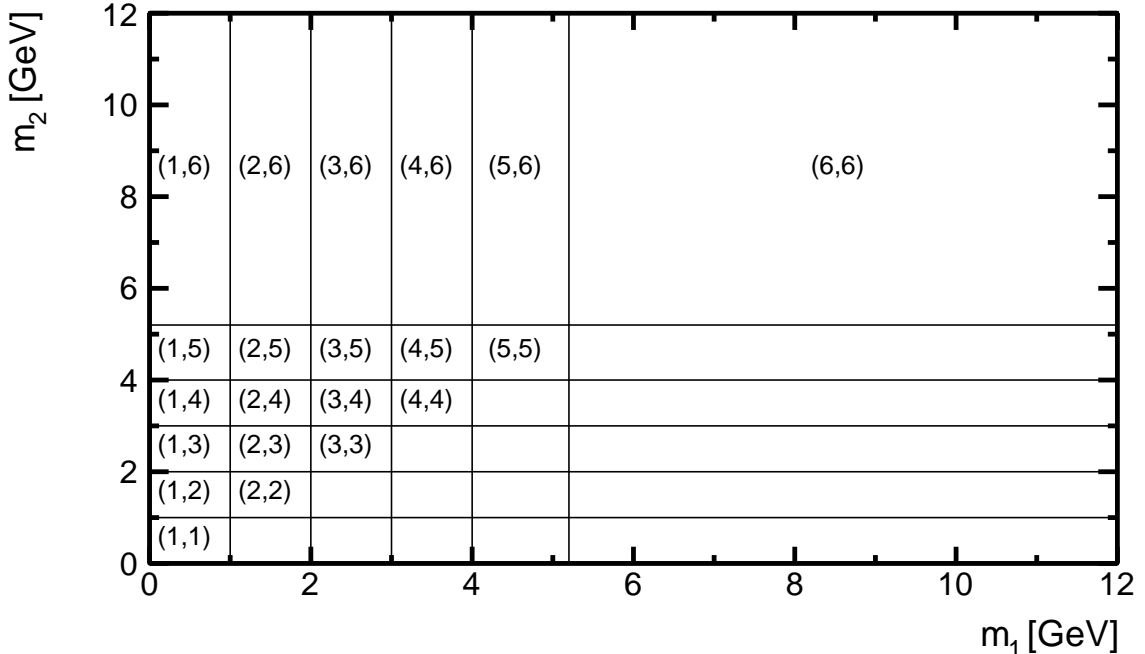

Figure 2: Binning of the 2D (m_1, m_2) distribution.

6   Background modeling

As mentioned in Section 5, QCD multijets constitute the dominant source of background, with small contributions coming from processes such as $t\bar{t}$, Z+jets, W+jets, diboson production. To model the shape of the 2D (m_1, m_2) distribution of the background in the SR, a binned template is constructed as:

$$f_{2D}(i, j) = C(i, j)\left(f_{1D}(i) f_{1D}(j) \right)^{\text{sym}} \tag{3}$$

where

- $f_{2D}(i, j)$ represents the content of the bin (i, j) in the normalized 2D invariant mass distribution of the muon-track systems;

- $f_{1D}(i)$ is the content of bin i in the normalized one-dimensional (1D) distribution of the muon-track invariant mass;

- $C(i, j)$ is a symmetric matrix, accounting for possible correlation between m_1 and m_2. The condition $C(i, j) = 1$ for all bins (i, j) would indicate an absence of correlation between m_1 and m_2. The elements of the matrix $C(i, j)$ are referred to as "correlation factors" henceforth.

Equation 3 includes a symmetrization operation, denoted by 'sym,' which is applied to the product of the one-dimensional distributions $f_{1D}(i)$ and $f_{1D}(j)$ and defined as follows:

$$\left(f_{1D}(i) f_{1D}(j) \right)^{\text{sym}} = \begin{cases} 2 f_{1D}(i) f_{1D}(j), & \text{if } i \neq j, \\ f_{1D}(i) f_{1D}(i), & \text{if } i = j. \end{cases} \tag{4}$$

As per Eq. 4, the contents of the nondiagonal bins (i, j) and (j, i) in the Cartesian product $f_{1D}(i) f_{1D}(j)$ are summed up to ensure that all events are accurately accounted for in the 2D (m_1, m_2) distribution, thereby maintaining the correct ordering of the muon-track invariant masses.

The normalization of the background is left unconstrained prior to the extraction of the signal.

In order to derive and validate the modeling of $f_{1D}(i)$ and $C(i, j)$, multiple control regions (CRs) are defined based on the variations in the isolation criteria applied to one or both muon-track pairs. These isolation criteria are defined by the number of tracks within a cone of $\Delta R = 0.5$ around the muon momentum direction. The two muons are categorized as the "first muon" and "second muon" based on these criteria. A summary of the CRs used to derive and validate the modeling of the background shape, along with the specifications for the first and second muon, is presented in Table 3.

6.1   Modeling of $f_{1D}(i)$

The $f_{1D}(i)$ distribution is modeled using the N_{23} CR. This CR comprises events that pass the SC dimuon selection criteria and include only one a_1 candidate, formed by an isolated "signal" track and a muon (referred to as the first muon). The invariant mass of this first muon and its associated track is used to construct the $f_{1D}(i)$ distribution. The second muon in the event must be accompanied by either two or three nearby "isolation" tracks. Simulations indicate that the N_{23} CR is enriched in QCD events, with less than 5% events coming from non-QCD backgrounds. The modeling of $f_{1D}(i)$ is based on the assumption that the kinematic distributions of the muon-track system forming the a_1 candidate are weakly affected by the isolation

Table 3: Control regions used to construct and validate the background model. The symbols N_{iso} and N_{sig} denote the number of "isolation" and "signal", respectively, within a cone of $\Delta R = 0.5$ around the muon momentum direction. In cases where N_{sig} is not mentioned, there is no explicit requirement on the number of "signal" tracks. The last row defines the SR.

Control region	First μ	Second μ	Purpose
N_{23}	$N_{\text{sig}} = 1$, $N_{\text{iso}} = 1$	$N_{\text{iso}} = 2,3$	Determination of $f_{1\text{D}}(i)$
$N_{\text{iso},2} = 1$	$N_{\text{sig}} \geq 1$, $N_{\text{iso}} > 1$	$N_{\text{sig}} = 1$, $N_{\text{iso}} = 1$	Validation and systematic uncertainty estimate of $f_{1\text{D}}(i)$
$N_{\text{iso},2} = 2,3$	$N_{\text{sig}} \geq 1$, $N_{\text{iso}} > 1$	$N_{\text{iso}} = 2,3$	Validation and systematic uncertainty estimate of $f_{1\text{D}}(i)$
Loose-Iso	$N_{\text{sig}} = 1$, $N_{\text{iso}} = 3,4$	$N_{\text{sig}} = 1$, $N_{\text{iso}} = 3,4$	Determination of $C(i,j)$
Signal region	$N_{\text{sig}} = 1$, $N_{\text{iso}} = 1$	$N_{\text{sig}} = 1$, $N_{\text{iso}} = 1$	Signal extraction

criteria applied to the second muon, implying, therefore, that the $f_{1\text{D}}(i)$ distribution in the SR is similar to that in the N_{23} CR.

A direct test of this assumption is not conclusive because of the limited size of the simulated events. Therefore, the hypothesis is verified using additional control regions labeled $N_{\text{iso},2} = 1$ and $N_{\text{iso},2} = 2,3$. Events are selected in these CRs if the first muon has more than one "isolation" track ($N_{\text{iso}} > 1$), with at least one of these "isolation" tracks also fulfilling the criteria for "signal" tracks. As more than one of these tracks can qualify the requirements to be a "signal" track, two scenarios are evaluated, using either the "signal" track with the lowest p_{T} ("softest") or the highest p_{T} ("hardest") to compute the muon-track invariant mass. If only one "signal" track is found around the first muon, it serves as both the "softest" and "hardest" track. For the second muon, two isolation scenarios are considered: one where the second muon has only one "signal" track, making the muon-track system isolated as in the SR (CR $N_{\text{iso},2} = 1$) and another where it has two or three "isolation" tracks as in the N_{23} region (CR $N_{\text{iso},2} = 2,3$). The invariant mass distributions of the first muon and its softest or hardest accompanying track are then compared between the two different isolation scenarios of the second muon. The results of this study are illustrated in Fig. 3. In both cases, the invariant mass distributions differ in each bin by less than 7%, suggesting that the invariant mass of the muon-track system forming an a_1 candidate is not highly sensitive to the isolation requirement on the second muon. To address any systematic effects on the modeling of the $f_{1\text{D}}(i)$ distribution in the N_{23} region, the observed differences are treated as a shape uncertainty in the normalized $f_{1\text{D}}(i)$ template.

Figure 4 presents the normalized invariant mass distribution of the muon-track system for data selected in the SR and for the background model derived from the N_{23} CR. The data and background distributions are compared to the signal distributions obtained from simulation for four representative mass hypotheses, $m_{a_1} = 5, 8, 12,$ and $15\,\text{GeV}$. The invariant mass of the muon-track system demonstrates higher discrimination power between the background and the signal at higher m_{a_1}. For lower masses, the signal shape becomes more similar to the background, thereby reducing the discrimination power.

6.2 Modeling of $C(i,j)$

The correlation factor $C(i,j)$ is determined using a different control region labeled Loose-Iso, which is non-overlapping with the SR. This CR consists of events containing two SC muons that meet the identification and kinematic selection criteria detailed in Section 5. In this CR,
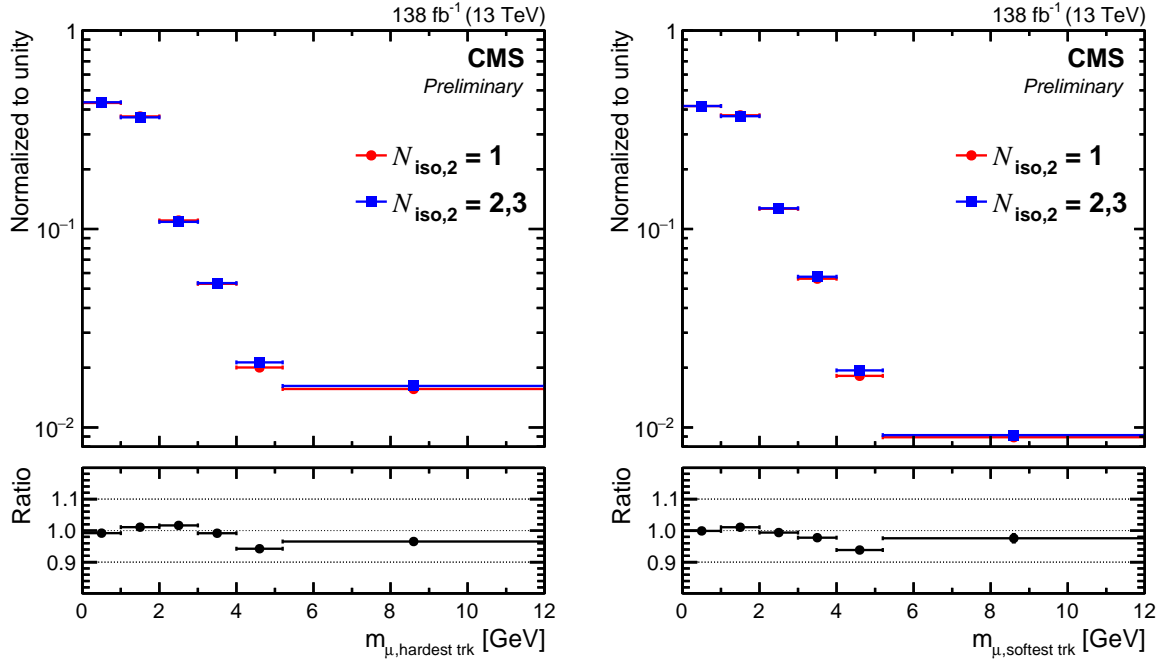
Figure 3: The observed invariant mass distribution, normalized to unity, of the first muon and the softest (left) or hardest (right) accompanying "signal" track for different isolation requirements imposed on the second muon: one "isolation" track ($N_{\text{iso,2}} = 1$; circles) or two to three "isolation" tracks ($N_{\text{iso,2}} = 2, 3$).

each muon must have three or four nearby tracks, one of which must be a "signal" track and the rest "isolation" tracks. Simulation predicts that QCD multijet events dominate in this CR, comprising approximately 99% of the selected events. The events selected in this region are used to construct the normalized distributions, $f_{\text{2D}}(i, j)$. The correlation factors $C(i, j)$ are then derived using Eq. (3) as:

$$C(i, j) = \frac{f_{\text{2D}}(i, j)}{(f_{\text{1D}}(i) f_{\text{1D}}(j))^{\text{sym}}}, \tag{5}$$

where $f_{\text{1D}}(i)$ is the 1D normalized distribution with two entries per event (m_1 and m_2). Figure 5 shows the correlation factors $C(i, j)_{\text{data}}^{\text{CR}}$ obtained from the data in the Loose-Iso CR.

To estimate $C(i, j)$ in data in the signal region, the correlation factors derived with data in the Loose-Iso CR are corrected for the difference in $C(i, j)$ between the signal region and the Loose-Iso CR by comparing samples of simulated background events. The correlation factors estimated from simulation in the signal region, $C(i, j)_{\text{MC}}^{\text{SR}}$, and the Loose-Iso CR, $C(i, j)_{\text{MC}}^{\text{CR}}$, are shown in Fig. 6 (top and bottom panels, respectively).

The correlation factors in data in the SR, $C(i, j)_{\text{data}}^{\text{SR}}$, are then computed as

$$C(i, j)_{\text{data}}^{\text{SR}} = C(i, j)_{\text{data}}^{\text{CR}} \frac{C(i, j)_{\text{MC}}^{\text{SR}}}{C(i, j)_{\text{MC}}^{\text{CR}}}, \tag{6}$$

Several systematic uncertainties can influence the correlation factors derived from simulated events:
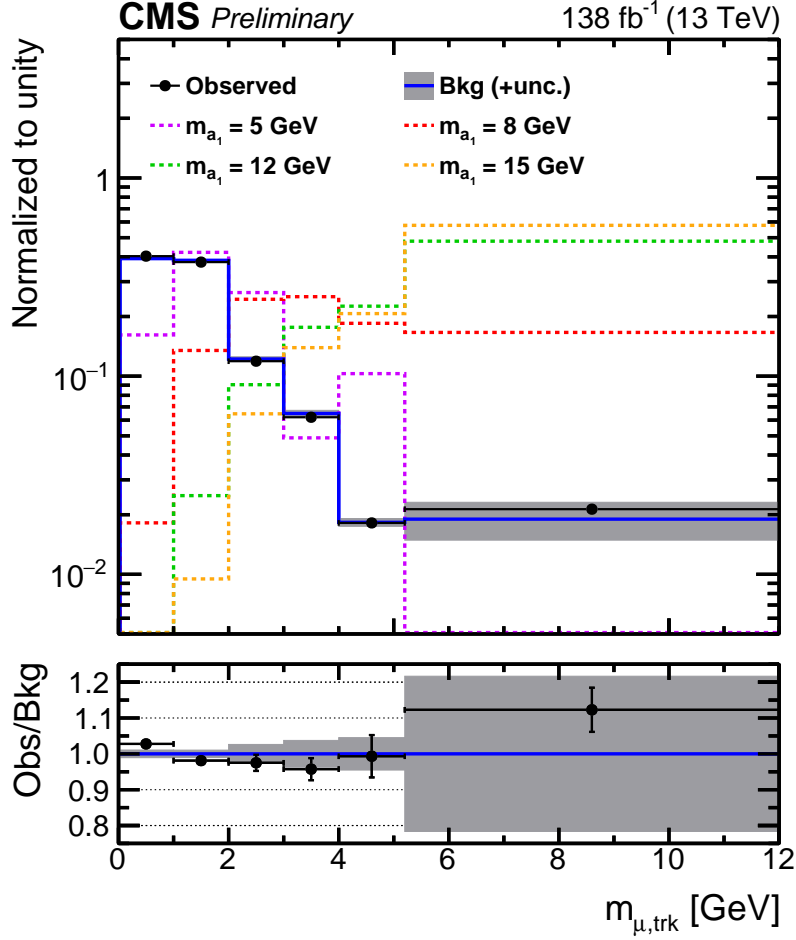
Figure 4: Normalized invariant mass distribution of the muon-track system for events passing the signal selection. Observed events are shown as black points with error bars. The background model in blue is derived from the N_{23} control region. Also shown are normalized distributions from signal simulations for four mass hypotheses, $m_{a_1} = 5, 8, 12,$ and $15\,\text{GeV}$ (dashed histograms). Signal distributions include both the $2\mu2\tau$ and 4τ contributions. Each event contributes two entries, corresponding to the two muon-track systems in each event that pass the selection. The lower panel shows the ratio of observed to expected background events in each bin. The grey shaded area represents the uncertainty of the background model.

- Uncertainty in parton shower scale: Variations in the modeling of initial and final state radiation (ISR and FSR) during parton showering can impact the reconstructed muon-track masses and their correlations in events where an a_1 candidate is mimicked by a hadronic jet, leading to potential deviations in $C(i, j)$. To account for this, the parton shower scale is varied up and down by a factor of 2 and 0.5, respectively.

- Uncertainty in the relative fraction of non-QCD events: To account for potential inaccuracies in the estimates of $C(i, j)$ due to the limited understanding of the contribution of non-QCD events, the non-QCD background fraction is allowed to vary by $\pm 50\%$. After applying this variation, the non-QCD fraction, depending on its initial value, can range from 0% to 4.8%.

Shape-altering uncertainties in the estimation of $C(i, j)_{\text{data}}^{\text{SR}}$ are incorporated by varying the correlation factors $C(i, j)_{\text{MC}}^{\text{SR}}$ and $C(i, j)_{\text{MC}}^{\text{CR}}$ based on above-mentioned systematic shifts.
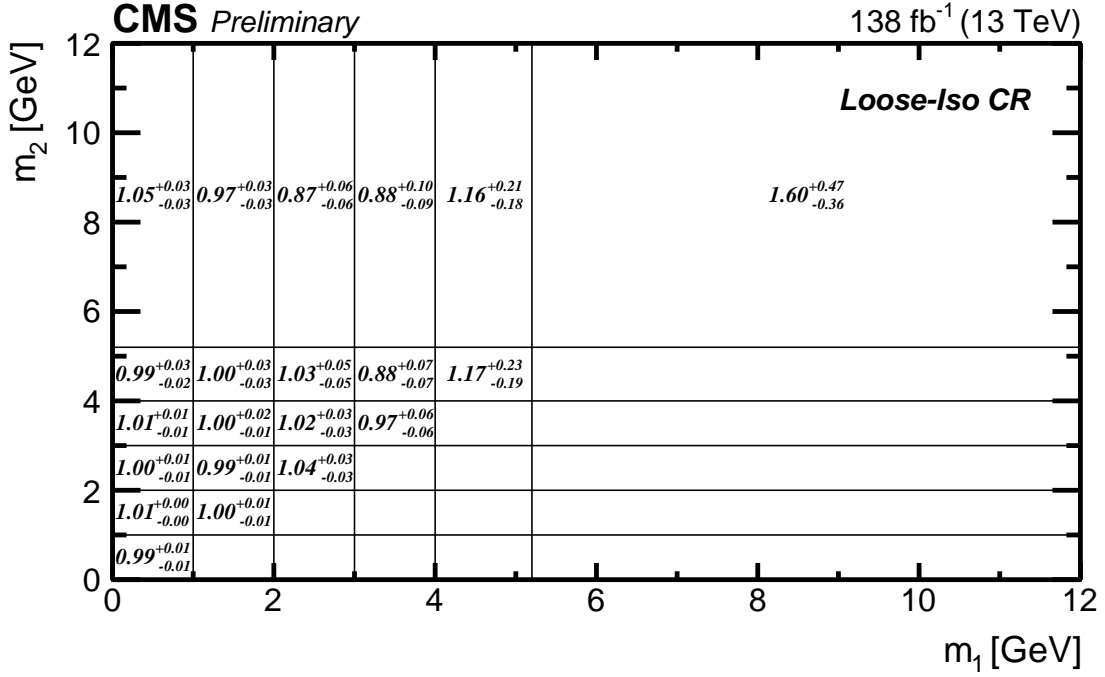
Figure 5: The correlation factors $C(i,j)^{\mathrm{CR}}_{\mathrm{data}}$ with statistical uncertainties.

7 Signal modeling

The signal model is constructed using simulated samples of the $H \rightarrow a_1 a_1 \rightarrow 4\tau$ and $H \rightarrow a_1 a_1 \rightarrow 2\mu 2\tau$ decays. The analysis probes the signal strength modifier, defined as the product of the measured signal cross section and the branching fraction into the 4τ final state, $\mathcal{B}(H \rightarrow a_1 a_1)\mathcal{B}^2(a_1 \rightarrow \tau\tau)$, relative to the value predicted by the SM for the inclusive cross section for H boson production. The relative contributions from different Higgs boson production modes are determined by the corresponding cross sections predicted by the SM. The contribution from the $H \rightarrow a_1 a_1 \rightarrow 2\mu 2\tau$ decay is computed under the assumption that the partial widths of the $a_1 \rightarrow \tau\tau$ and $a_1 \rightarrow \mu\mu$ decays satisfy Eq. (1).

The invariant mass distribution of the muon-track system in the $a_1 \rightarrow \mu\mu$ decay channel peaks at the nominal a_1 boson mass. In contrast, the reconstructed mass of the muon-track system in the $a_1 \rightarrow \tau\tau$ decay is generally lower and has a larger dispersion due to the presence of undetected neutrinos. As a result, the $H \rightarrow a_1 a_1 \rightarrow 2\mu 2\tau$ signal samples have a considerably different shape in the (m_1, m_2) distribution compared to the $H \rightarrow a_1 a_1 \rightarrow 4\tau$ signal samples. Figure 7 illustrates the (m_1, m_2) distributions, unrolled into a one-dimensional array, for the $H \rightarrow a_1 a_1 \rightarrow 4\tau$ and $H \rightarrow a_1 a_1 \rightarrow 2\mu 2\tau$ signal samples for the mass hypotheses $m_{a_1} = 5$, 8, 12 and 15 GeV. These signal distributions are normalized assuming the SM Higgs boson production rate and a branching fraction $\mathcal{B}(H \rightarrow a_1 a_1)\mathcal{B}^2(a_1 \rightarrow \tau\tau)$ of 0.05.

8 Systematic uncertainties

Several sources of uncertainties, both of statistical and systematic origin, are considered in the analysis. Bin-by-bin statistical uncertainties in the signal and background templates are incorporated into the analysis using the Barlow-Beeston-lite method [65]. These uncertainties arise from the limited size of data samples in the control regions used for background modeling and simulated samples of background and signal processes. Additionally, multiple systematic
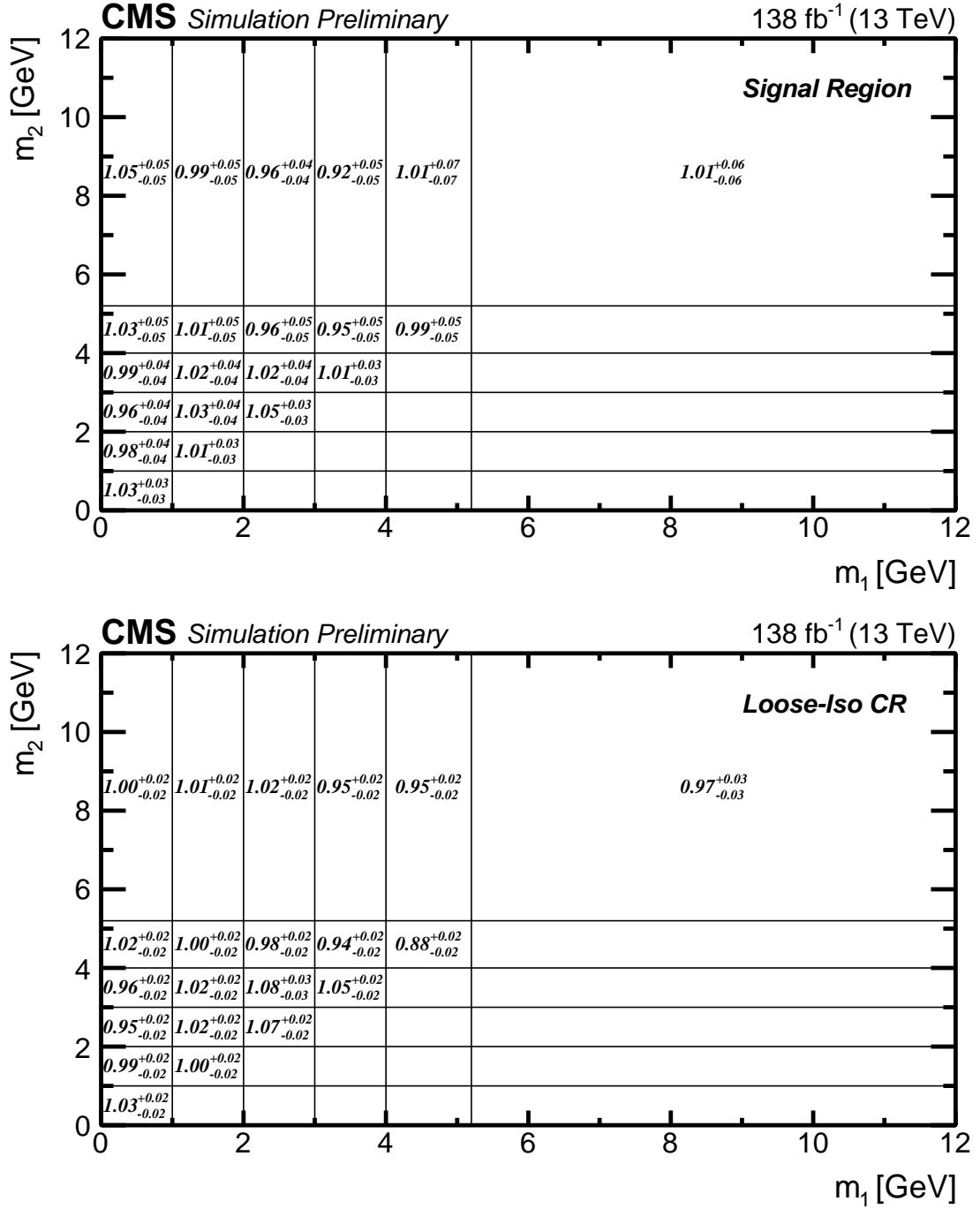
CMS *Simulation Preliminary*   138 fb^{-1} (13 TeV)

Signal Region

$1.05^{+0.05}_{-0.05}$ $0.99^{+0.05}_{-0.05}$ $0.96^{+0.04}_{-0.04}$ $0.92^{+0.05}_{-0.05}$ $1.01^{+0.07}_{-0.07}$ $1.01^{+0.06}_{-0.06}$

$1.03^{+0.05}_{-0.05}$ $1.01^{+0.05}_{-0.05}$ $0.96^{+0.05}_{-0.05}$ $0.95^{+0.05}_{-0.05}$ $0.99^{+0.05}_{-0.05}$

$0.99^{+0.04}_{-0.04}$ $1.02^{+0.04}_{-0.04}$ $1.02^{+0.04}_{-0.04}$ $1.01^{+0.03}_{-0.03}$

$0.96^{+0.04}_{-0.04}$ $1.03^{+0.04}_{-0.04}$ $1.05^{+0.03}_{-0.03}$

$0.98^{+0.04}_{-0.04}$ $1.01^{+0.03}_{-0.03}$

$1.03^{+0.03}_{-0.03}$

CMS *Simulation Preliminary*   138 fb^{-1} (13 TeV)

Loose-Iso CR

$1.00^{+0.02}_{-0.02}$ $1.01^{+0.02}_{-0.02}$ $1.02^{+0.02}_{-0.02}$ $0.95^{+0.02}_{-0.02}$ $0.95^{+0.02}_{-0.02}$ $0.97^{+0.03}_{-0.03}$

$1.02^{+0.02}_{-0.02}$ $1.00^{+0.02}_{-0.02}$ $0.98^{+0.02}_{-0.02}$ $0.94^{+0.02}_{-0.02}$ $0.88^{+0.02}_{-0.02}$

$0.96^{+0.02}_{-0.02}$ $1.02^{+0.02}_{-0.02}$ $1.08^{+0.03}_{-0.03}$ $1.05^{+0.02}_{-0.02}$

$0.95^{+0.02}_{-0.02}$ $1.02^{+0.02}_{-0.02}$ $1.07^{+0.02}_{-0.02}$

$0.99^{+0.02}_{-0.02}$ $1.00^{+0.02}_{-0.02}$

$1.03^{+0.02}_{-0.02}$

Figure 6: The correlation factors $C(i,j)^{\text{SR}}_{\text{MC}}$ (upper) and $C(i,j)^{\text{CR}}_{\text{MC}}$ (lower) with statistical uncertainties.

uncertainties are included, which can be classified into two categories: uncertainties related to the background and uncertainties related to the signal.

8.1   Uncertainties related to the background

The shape of the background in the 2D (m_1, m_2) distribution is modeled according to Eq. (3). The 2D distribution is affected by the shape uncertainty in the 1D template $f_{1\text{D}}(i)$, described in
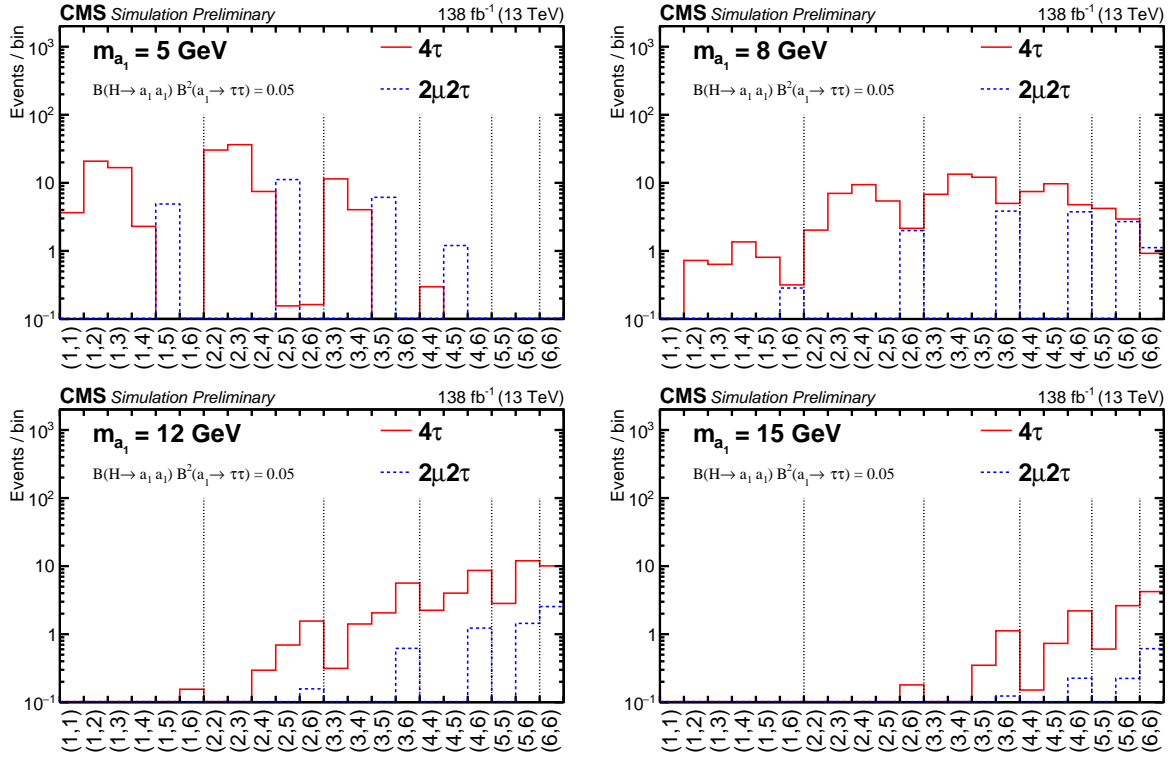
Figure 7: The signal $f_{2D}(i, j)$ templates for mass hypothesis $m_{a_1} = 5\,\text{GeV}$ (upper left), $8\,\text{GeV}$ (upper right), $12\,\text{GeV}$ (lower left) and $15\,\text{GeV}$ (lower right). The H $\rightarrow a_1 a_1 \rightarrow 2\mu2\tau$ (blue histogram) and H $\rightarrow a_1 a_1 \rightarrow 4\tau$ (red histogram) contributions are shown. The distributions are normalized assuming SM H production cross section and $\mathcal{B}(\text{H} \rightarrow a_1 a_1)\mathcal{B}^2(a_1 \rightarrow \tau\tau) = 0.05$. The bin notation follows that of Fig. 2.

Section 6.1, which accounts for any potential bias introduced by estimating the 1D distribution in the N_{23} CR. The effect of this uncertainty on the yield in bins of the background template is utmost 9%. The background shape is further impacted by uncertainties related to the extrapolation of the correlation factors $C(i, j)$ from the Loose-Iso CR to the SR, which stem from systematic variations in the modeling of ISR and FSR and the non-QCD background fraction in the MC simulations as described in Section 6.2. The associated shape uncertainties are determined by comparing the correlation factors derived from simulated events in the signal region and the Loose-Iso CR, taking into account these systematic variations. The systematics associated with ISR, FSR, and non-QCD contributions induce a variation of up to 1%, 2%, and 6%, respectively, in the background yield for individual bins.

8.2 Uncertainties related to signal

The integrated luminosities for the 2016, 2017, and 2018 data-taking years have individual uncertainties in the range 1.2–2.5% [66–68], while the overall uncertainty for the 2016–2018 period is 1.6%.

Uncertainties in muon identification and trigger efficiencies, as determined using a tag-and-probe method [69], are estimated to be 1.5% per muon. The efficiencies of track selection and muon-track isolation are evaluated in a study of Z $\rightarrow \tau\tau$ events where one tau decays to a muon, while the other decays into an isolated track in a 1-prong decay. This track meets the same selection criteria as in the primary analysis. The resulting uncertainties affect the shape

of the signal estimate and alter the overall signal yield by 10–20%.

During the 2016–2017 data-taking periods, a timing shift in the ECAL L1 trigger inputs in the forward endcap region ($|\eta| > 2.4$) caused inefficiencies by incorrectly associating events with the previous bunch crossing [39]. A correction for this effect, determined using an unbiased data sample, is applied to simulated samples, accompanied by normalization-altering uncertainties ranging between 0.1–2.8%, depending on the mass point and sample.

The uncertainties in measuring the b tagging efficiency are applied separately to heavy-flavor and light-flavor jets in simulated samples as described in Ref. [61]. These uncertainties are divided into components specific to the data-taking and components correlated across periods. For ggF, VBF, and VH signal samples, the b tagging uncertainties lead to variations in the yield between 0.2–0.5%, whereas for the $t\bar{t}H$ samples, the variations range from 4 to 6%.

Theoretical uncertainties impact the kinematic distributions of the H boson, particularly its p_T spectrum, thereby affecting signal acceptance. The uncertainty due to missing higher-order corrections in the ggF process is estimated using the HQT program by varying the renormalization (μ_R) and factorization (μ_F) scales. The Higgs boson p_T-dependent k-factors are recomputed according to these variations and applied to the simulated signal samples. The resulting effect on the signal acceptance varies between 2.5 and 3.5%, depending on m_{a_1}. Similarly, uncertainties in signal acceptance for VBF, VH, and $t\bar{t}H$ production processes are computed, with impacts ranging from 1 to 3%, depending on the process and the mass of a_1.

The HQT program is also used to evaluate uncertainties arising from the choice of PDFs. The nominal k-factors for p_T spectrum of the H boson are computed using the NNPDF3.1 PDF set [70]. Variations within the uncertainties of the NNPDF3.1 PDFs alter the signal acceptance by approximately 1% while using the CTEQ6L1 PDF set [71] results in a change of about 0.7%. The impact of PDF uncertainties on the acceptance for the VBF, VH, and $t\bar{t}H$ production processes is estimated in a similar way, resulting in a 2% uncertainty.

The bin-by-bin statistical uncertainties, primarily driven by limited statistics of data in the Loose-Iso control region, constitute the dominant uncertainties across all signal mass hypotheses. Additionally, shape uncertainties related to the modeling $f_{1D}(i)$ and $C(i,j)$ have substantial effects. For higher pseudoscalar masses, the uncertainty associated with track selection and muon isolation efficiency also becomes significant.

9 Results

The results discussed in this section are determined using the CMS statistical analysis tool COMBINE [72], which is based on the ROOFIT [73] and ROOSTATS [74] frameworks.

The signal is extracted with a binned maximum-likelihood fit applied to the (m_1, m_2) distribution. The normalization of both signal and background is allowed to float freely in the fit. Systematic uncertainties affecting the normalization of the signal templates are incorporated into the fit via nuisance parameters with log-normal distributions. Shape-altering systematic uncertainties are modeled by nuisance parameters whose variations cause continuous morphing of the signal or background template shapes and are assigned Gaussian prior probability density functions. Bin-by-bin statistical uncertainties are taken into account using the Barlow-Beeston-lite approach [65]. For each probed mass of the a_1 boson, the (m_1, m_2) distribution is fitted with the sum of two templates, one for the signal and one for the background. No significant excess of events over the background expectation is observed.

Figure 8 displays the distribution of (m_1, m_2), where the notation for the bins follows that of Fig. 2. For illustrative purposes, the background distribution is normalized by fitting the observed data under the background-only hypothesis. Expectations for the signal for $m_{a_1} = 5, 8, 12,$ and 15 GeV are also shown. The signal normalization is calculated assuming the SM production rate for the H boson and a branching fraction of 5% for the $H \rightarrow a_1 a_1 \rightarrow 4\tau$ decays.
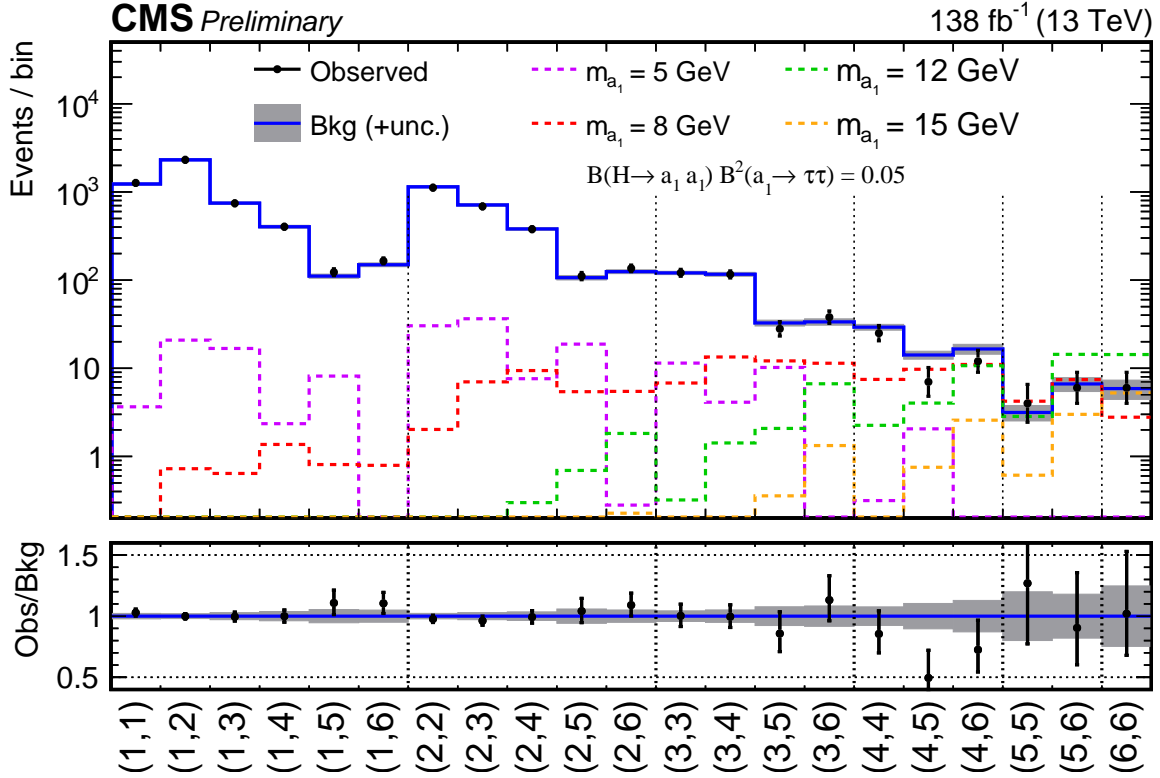

Figure 8: The (m_1, m_2) in one-row distribution used to extract the signal. The observed number of events is represented by data points with error bars. The background with its uncertainty is shown as the blue histogram with the shaded error band. The normalization for the background is obtained by fitting the observed data under the background-only hypothesis. Signal expectations for the 4τ and $2\mu2\tau$ final states are shown as dashed histograms for the mass hypotheses $m_{a_1} = 5, 8, 12,$ and 15 GeV. The relative normalization of the 4τ and $2\mu2\tau$ final states are given by Eq. (1) as explained in Section 7. The signal normalization is computed assuming that the H boson is produced in pp collisions with a rate predicted by the SM and decays into $a_1 a_1 \rightarrow 4\tau$ final state with the branching fraction of 5%. The lower plot shows the ratio of the observed data events to the expected background yield in each bin of the (m_1, m_2) distribution.

The results of the analysis are used to set model-independent upper limits at 95% CL on the product of the cross section and branching fraction, $\sigma(pp \rightarrow H + X)\mathcal{B}(H \rightarrow a_1 a_1)\mathcal{B}^2(a_1 \rightarrow \tau\tau)$, relative to the inclusive SM H boson production cross section, σ_{SM}. Figure 9 shows the obtained observed and expected upper limits. The observed limits range from 0.007 at $m_{a_1} = 11$ GeV to 0.079 at $m_{a_1} = 4$ GeV. The expected upper limits range from 0.011 at $m_{a_1} = 11$ GeV to 0.066 at $m_{a_1} = 4$ GeV. The observed limits are compatible with the expected limits within two standard deviations in the entire range of m_{a_1} considered. The degradation of the analysis sensitivity towards lower values of m_{a_1} is caused by the increase of the background towards low invariant masses of the muon-track systems, as illustrated in Figs. 4 and 8. As m_{a_1} increases, the average angular separation between the decay products of the a_1 boson increases. Consequently, the
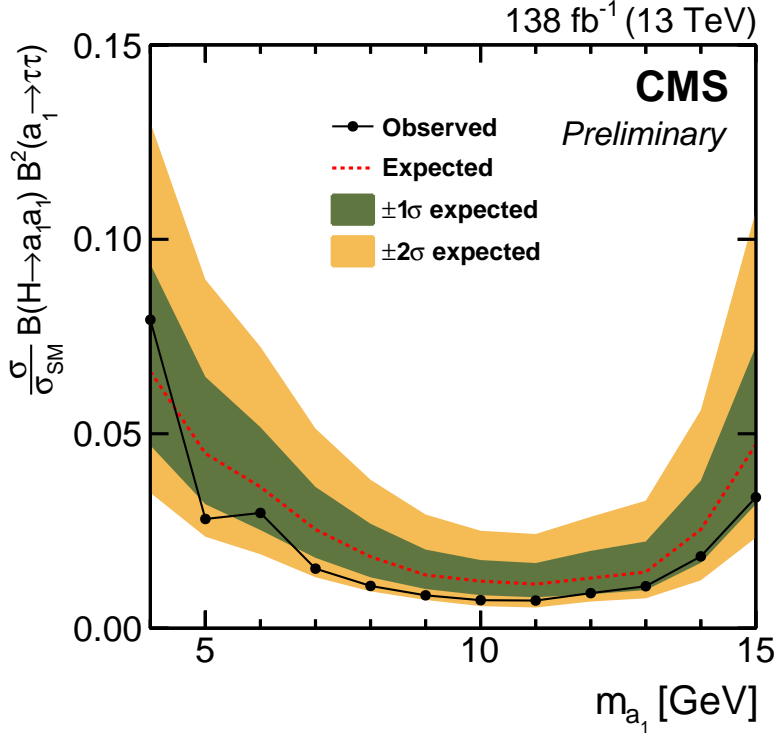
Figure 9: The observed and expected upper limits at 95% confidence level on the product of the signal cross section and the branching fraction $\sigma(\mathrm{pp} \to \mathrm{H} + \mathrm{X})\mathcal{B}(\mathrm{H} \to \mathrm{a_1 a_1})\mathcal{B}^2(\mathrm{a_1} \to \tau\tau)$, relative to the inclusive Higgs boson production cross section σ_{SM} predicted in the SM. The green and yellow bands indicate the regions containing 68% and 95% of the distribution of limits expected under the background-only hypothesis.

efficiency of the signal selection decreases due to the requirement that the muon and the track from the $\mathrm{a_1} \to \tau_\mu \tau_{1\text{-prong}}$ or $\mathrm{a_1} \to \mu\mu$ decay must be within a cone of $\Delta R = 0.5$. This explains the reduced sensitivity at higher values of $m_{\mathrm{a_1}}$.

The results are also reinterpreted in the context of 2HDM+S models. The upper limits on the signal strength are translated into constraints on $\sigma(\mathrm{pp} \to \mathrm{H} + \mathrm{X})\mathcal{B}(\mathrm{H} \to \mathrm{a_1 a_1})$ by scaling them with the predicted branching fraction $\mathcal{B}(\mathrm{a_1} \to \tau\tau)$. The branching fraction, which depends on the model type, the pseudoscalar mass, and $\tan\beta$, is calculated using the decay width expressions from Ref. [75]. Figure 10 shows the observed and expected 95% CL upper limits on $\sigma(\mathrm{pp} \to \mathrm{H} + \mathrm{X})\mathcal{B}(\mathrm{H} \to \mathrm{a_1 a_1})$ obtained for the four types of 2HDM+S models for benchmark values of $\tan\beta$ corresponding to scenarios where the $\mathrm{a_1} \to \tau\tau$ decay has a sizeable branching fraction. Among the scenarios considered, the Type III 2HDM+S model for $\tan\beta = 2$ provides the most stringent limits across all mass points between 4 and 15 GeV. The observed limits range from 0.01 at $m_{\mathrm{a_1}} = 9$ GeV to 0.36 at $m_{\mathrm{a_1}} = 4$ GeV. For Type II models, for $\tan\beta = 5$, tight constraints are obtained for masses up to 9 GeV. The observed limits lie between 0.013 and 0.09 in this range. Above 9 GeV, the decays of $\mathrm{a_1}$ to bottom quarks overwhelm its decays to taus, making the analysis less sensitive. The branching fraction in Type I is independent of $\tan\beta$, leading to a constant exclusion range across different values of this parameter. In this model, the branching fraction to taus is less enhanced as it has to compete with other channels like $\mathrm{c\bar{c}}$ and $\mathrm{b\bar{b}}$. Thus, the analysis provides less stringent constraints on $\sigma(\mathrm{pp} \to \mathrm{H} + \mathrm{X})\mathcal{B}(\mathrm{H} \to \mathrm{a_1 a_1})$ for Type I. For Type IV, the analysis is only sensitive for $\tan\beta < 1$, as for higher values of $\tan\beta$, the decays to quarks dominate in the considered mass range.

The peak-like shapes seen in Fig. 10 occur in the mass regions where quarkonium states, such as η_c and η_b, are found. In these regions, the mixing of a_1-quarkonium states plays a crucial role, leading to a sudden increase in the hadronic decay width due to non-perturbative QCD effects. This results in a significant decrease in the branching fractions to unbounded systems, such as $\tau\tau$. The mixing of a_1 with η_c and η_b is significantly amplified in scenarios where the couplings of a_1 to c- and b-quarks, respectively, are predominant. Further details of the a_1-quarkonium mixing can be found in Refs. [75, 76]. As a result of the mixing, the analysis fails to provide tight constraints in these mass regions.

Upper limits at 95% CL are also set on $\sigma(pp \rightarrow H + X)\mathcal{B}(H \rightarrow a_1a_1)$, relative to σ_{SM}, as a function of $\tan\beta$ for benchmark pseudoscalar masses. Figures 11 and 12 present the limits obtained for Type II and Type III 2HDM+S, respectively, for m_{a_1} = 5, 8, 12, and 15 GeV. In both
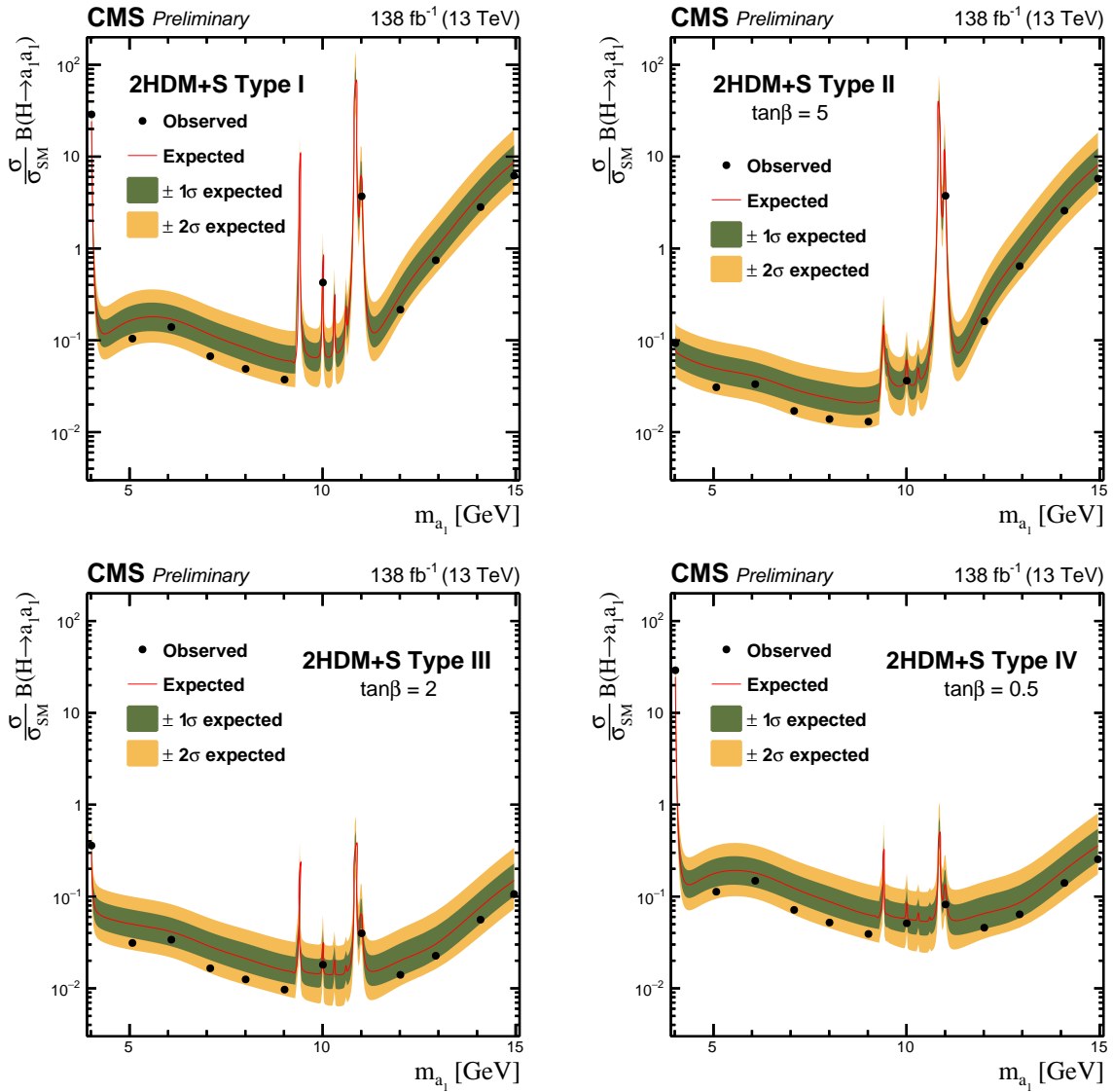

Figure 10: The observed and expected upper limits at 95% CLs on $\sigma(pp \rightarrow H + X)\mathcal{B}(H \rightarrow a_1a_1)$, relative to σ_{SM}, as a function of m_{a_1} for different 2HDM+S models for benchmark $\tan\beta$ values: Type I ($\tan\beta$ independent; upper left), Type II ($\tan\beta = 5$; upper right), Type III ($\tan\beta = 2$; lower left) and Type IV ($\tan\beta = 0.5$; lower right).

models, the analysis is able to set stringent constraints for $\tan\beta > 1$, where the couplings to taus are enhanced. For $\tan\beta < 1$, the decays to quarks dominate, suppressing the $a_1 \to \tau\tau$ decays, resulting in weaker limits. The Type III 2HDM+S model provides the best constraints for $\tan\beta > 1$ across all considered mass points. In the Type II model, tight constraints are obtained for $m_{a_1} = 5$ and $8\,\text{GeV}$, but the limits deteriorate for higher masses, due to the enhanced Yukawa coupling to b-quarks. The observed deterioration of the limits at lower and higher masses for both models can be directly related to the trends observed in the model-independent results, with the enhanced b-quark coupling playing an additional role in weakening the limits for higher masses in the Type II model.
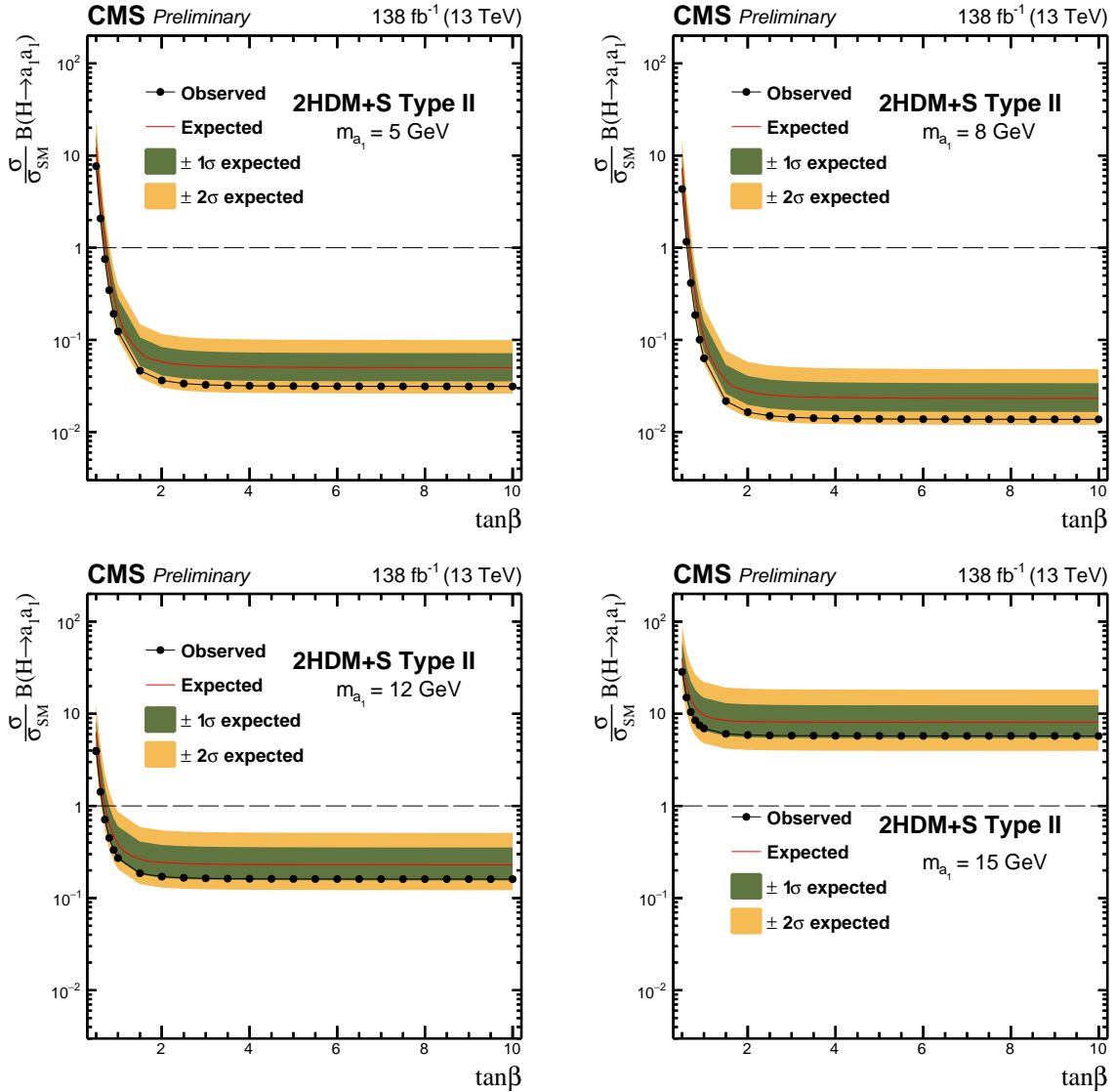

Figure 11: The observed and expected 95% CL upper limits on $\sigma(\text{pp} \to \text{H} + \text{X})\mathcal{B}(\text{H} \to a_1 a_1)$, relative to σ_{SM}, as a function of $\tan\beta$ for the Type II 2HDM+S model for: $m_{a_1} = 5\,\text{GeV}$ (upper left), $m_{a_1} = 8\,\text{GeV}$ (upper right), $m_{a_1} = 12\,\text{GeV}$ (lower left) and $m_{a_1} = 15\,\text{GeV}$ (lower right).
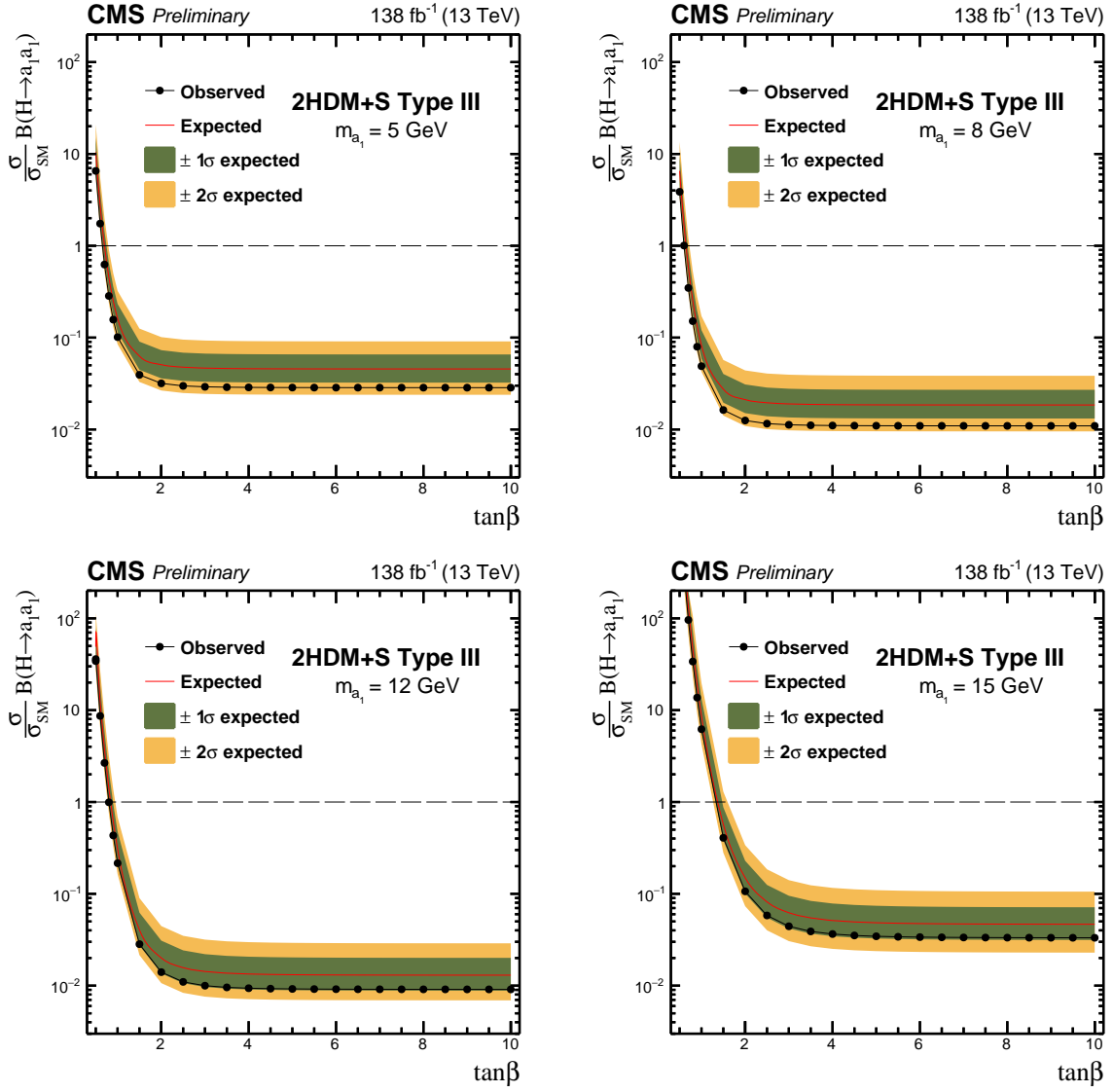
Figure 12: The observed and expected 95% CL upper limits on $\sigma(\mathrm{pp} \to \mathrm{H} + \mathrm{X})\mathcal{B}(\mathrm{H} \to \mathrm{a}_1\mathrm{a}_1)$, relative to σ_{SM}, as a function of $\tan\beta$ for the Type III 2HDM+S model for: $m_{\mathrm{a}_1} = 5\,\mathrm{GeV}$ (upper left), $m_{\mathrm{a}_1} = 8\,\mathrm{GeV}$ (upper right), $m_{\mathrm{a}_1} = 12\,\mathrm{GeV}$ (lower left) and $m_{\mathrm{a}_1} = 15\,\mathrm{GeV}$ (lower right).

10 Summary

A search for light pseudoscalar bosons (a_1) produced in decays of the 125 GeV Higgs boson (H) in final states with four taus or two muons and two taus is presented. The search is performed using data from proton-proton collisions at a center-of-mass energy of 13 TeV, collected by the CMS experiment at the LHC between 2016 and 2018 and corresponding to an integrated luminosity of 138 fb^{-1}. Pseudoscalar bosons with masses (m_{a_1}) in the range of 4 to 15 GeV are examined. The analysis is based on inclusive H boson production and targets the $H \rightarrow a_1 a_1 \rightarrow 4\tau/2\mu2\tau$ decay channels. Both channels are used in combination to constrain the product of the inclusive signal production cross section and the branching fraction into the 4τ final state, $\sigma(pp \rightarrow H + X)\mathcal{B}(H \rightarrow a_1 a_1)\mathcal{B}^2(a_1 \rightarrow \tau\tau)$. This is done by exploiting the linear dependence of the fermionic coupling strength of a_1 on the fermion mass. No significant excess in data over the expected standard model (SM) background is observed. Hence, upper limits on the product of the inclusive signal cross section and the branching fraction, $\sigma(pp \rightarrow H + X)\mathcal{B}(H \rightarrow a_1 a_1)\mathcal{B}^2(a_1 \rightarrow \tau\tau)$, relative to the SM H production cross section, σ_{SM}, are set at 95% confidence level. The observed limits range from 0.007 at $m_{a_1} = 11$ GeV to 0.079 at $m_{a_1} = 4$ GeV. The expected limits range from 0.011 at $m_{a_1} = 11$ GeV to 0.066 at $m_{a_1} = 4$ GeV. The results indicate significant improvement compared to the earlier similar CMS analysis at 13 TeV, exceeding the anticipated improvement resulting from the larger data sample alone. Sensitivity is enhanced by 2 to 4 times depending on the mass hypothesis, which can be attributed to the introduction of a veto for b tagged jets and the tightening of the impact parameters of the "isolation" tracks, both of which play a crucial role in background reduction. The results are also reinterpreted in the context of various types of 2HDM+S models. The tightest constraints on $\sigma(pp \rightarrow H + X)\mathcal{B}(H \rightarrow a_1 a_1)$, relative to σ_{SM} are provided for Type III 2HDM+S. For this scenario, regions of the phase space with $\tan \beta \geq 2$ are excluded for most m_{a_1}. For the Type II 2HDM+S model, stringent limits are observed for mass values between 4 and 9 GeV when $\tan \beta > 1$, indicating strong exclusion capabilities within this mass range.

References

[1] ATLAS Collaboration, "Observation of a new particle in the search for the standard model Higgs boson with the ATLAS detector at the LHC", *Phys. Lett. B* **716** (2012) 1, `doi:10.1016/j.physletb.2012.08.020`, `arXiv:1207.7214`.

[2] CMS Collaboration, "Observation of a new boson at a mass of 125 GeV with the CMS experiment at the LHC", *Phys. Lett. B* **716** (2012) 30, `doi:10.1016/j.physletb.2012.08.021`, `arXiv:1207.7235`.

[3] CMS Collaboration, "Observation of a new boson with mass near 125 GeV in pp collisions at $\sqrt{s}$ = 7 and 8 TeV", *JHEP* **06** (2013) 081, `doi:10.1007/JHEP06(2013)081`, `arXiv:1303.4571`.

[4] P. Fayet, "Supergauge invariant extension of the Higgs mechanism and a model for the electron and its neutrino", *Nucl. Phys. B* **90** (1975) 104, `doi:10.1016/0550-3213(75)90636-7`.

[5] P. Fayet, "Spontaneously broken supersymmetric theories of weak, electromagnetic and strong interactions", *Phys. Lett. B* **69** (1977) 489, `doi:10.1016/0370-2693(77)90852-8`.

[6] U. Ellwanger, C. Hugonie, and A. M. Teixeira, "The next-to-minimal supersymmetric standard model", *Phys. Rept.* **496** (2010) 1, `doi:10.1016/j.physrep.2010.07.001`, `arXiv:0910.1785`.

[7] M. Maniatis, "The next-to-minimal supersymmetric extension of the standard model reviewed", *Int. J. Mod. Phys. A* **25** (2010) 3505, `doi:10.1142/S0217751X10049827`, `arXiv:0906.0777`.

[8] T. D. Lee, "A theory of spontaneous T violation", *Phys. Rev. D* **8** (1973) 1226, `doi:10.1103/PhysRevD.8.1226`.

[9] G. C. Branco et al., "Theory and phenomenology of two-Higgs-doublet models", *Phys. Rept.* **516** (2012) 1, `doi:10.1016/j.physrep.2012.02.002`, `arXiv:1106.0034`.

[10] D. Curtin et al., "Exotic decays of the 125 GeV Higgs boson", *Phys. Rev. D* **90** (2014) 075004, `doi:10.1103/PhysRevD.90.075004`, `arXiv:1312.4992`.

[11] N. Arkani-Hamed, A. G. Cohen, E. Katz, and A. E. Nelson, "The littlest Higgs", *JHEP* **07** (2002) 034, `doi:10.1088/1126-6708/2002/07/034`, `arXiv:hep-ph/0206021`.

[12] M. Schmaltz and D. Tucker-Smith, "Little Higgs review", *Ann. Rev. Nucl. Part. Sci.* **55** (2005) 229, `doi:10.1146/annurev.nucl.55.090704.151502`, `arXiv:hep-ph/0502182`.

[13] S. Baum, M. Carena, N. R. Shah, and C. E. M. Wagner, "Higgs portals for thermal Dark Matter. EFT perspectives and the NMSSM", *JHEP* **04** (2018) 069, `doi:10.1007/JHEP04(2018)069`, `arXiv:1712.09873`.

[14] T. Alanne, K. Kainulainen, K. Tuominen, and V. Vaskonen, "Baryogenesis in the two doublet and inert singlet extension of the standard model", *JCAP* **08** (2016) 057, `doi:10.1088/1475-7516/2016/08/057`, `arXiv:1607.03303`.

[15] J. E. Kim and H. P. Nilles, "The mu Problem and the Strong CP Problem", *Phys. Lett. B* **138** (1984) 150, `doi:10.1016/0370-2693(84)91890-2`.

[16] S. Ramos-Sanchez, "The mu-problem, the NMSSM and string theory", *Fortsch. Phys.* **58** (2010) 748, `doi:10.1002/prop.201000058`, `arXiv:1003.1307`.

[17] ATLAS Collaboration, "A detailed map of Higgs boson interactions by the ATLAS experiment ten years after the discovery", *Nature* **607** (2022) 52, `doi:10.1038/s41586-022-04893-w`, `arXiv:2207.00092`. [Erratum: Nature 612, E24 (2022)].

[18] CMS Collaboration, "A portrait of the Higgs boson by the CMS experiment ten years after the discovery.", *Nature* **607** (2022) 60, `doi:10.1038/s41586-022-04892-x`, `arXiv:2207.00043`.

[19] ATLAS Collaboration, "Search for new light gauge bosons in Higgs boson decays to four-lepton final states in pp collisions at $\sqrt{s} = 8$ TeV with the ATLAS detector at the LHC", *Phys. Rev. D* **92** (2015), no. 9, 092001, `doi:10.1103/PhysRevD.92.092001`, `arXiv:1505.07645`.

[20] CMS Collaboration, "Search for a Non-Standard-Model Higgs Boson Decaying to a Pair of New Light Bosons in Four-Muon Final States", *Phys. Lett. B* **726** (2013) 564, `doi:10.1016/j.physletb.2013.09.009`, `arXiv:1210.7619`.

[21] CMS Collaboration, "A search for pair production of new light bosons decaying into muons", *Phys. Lett. B* **752** (2016) 146, `doi:10.1016/j.physletb.2015.10.067`, `arXiv:1506.00424`.

[22] CMS Collaboration, "Search for light bosons in decays of the 125 GeV Higgs boson in proton-proton collisions at $\sqrt{s} = 8$ TeV", *JHEP* **10** (2017) 076, `doi:10.1007/JHEP10(2017)076`, `arXiv:1701.02032`.

[23] CMS Collaboration, "Search for a very light NMSSM Higgs boson produced in decays of the 125 GeV scalar boson and decaying into τ leptons in pp collisions at $\sqrt{s} = 8$ TeV", *JHEP* **01** (2016) 079, `doi:10.1007/JHEP01(2016)079`, `arXiv:1510.06534`.

[24] ATLAS Collaboration, "Search for new phenomena in events with at least three photons collected in pp collisions at $\sqrt{s} = 8$ TeV with the ATLAS detector", *Eur. Phys. J. C* **76** (2016) 210, `doi:10.1140/epjc/s10052-016-4034-8`, `arXiv:1509.05051`.

[25] ATLAS Collaboration, "Search for Higgs boson decays to beyond-the-standard-model light bosons in four-lepton events with the ATLAS detector at $\sqrt{s} =$13 TeV", *JHEP* **06** (2018) 166, `doi:10.1007/JHEP06(2018)166`, `arXiv:1802.03388`.

[26] CMS Collaboration, "A search for pair production of new light bosons decaying into muons in proton-proton collisions at 13 TeV", *Phys. Lett. B* **796** (2019) 131, `doi:10.1016/j.physletb.2019.07.013`, `arXiv:1812.00380`.

[27] ATLAS Collaboration, "Search for Higgs bosons decaying to aa in the $\mu\mu\tau\tau$ final state in pp collisions at $\sqrt{s} = 8$ TeV with the ATLAS experiment", *Phys. Rev. D* **92** (2015) 052002, `doi:10.1103/PhysRevD.92.052002`, `arXiv:1505.01609`.

[28] CMS Collaboration, "Search for an exotic decay of the Higgs boson to a pair of light pseudoscalars in the final state of two muons and two τ leptons in proton-proton collisions at $\sqrt{s} =$ 13 TeV", *JHEP* **11** (2018) 018, `doi:10.1007/JHEP11(2018)018`, `arXiv:1805.04865`.

[29] CMS Collaboration, "Search for a light pseudoscalar Higgs boson in the boosted $\mu\mu\tau\tau$ final state in proton-proton collisions at $\sqrt{s} =$ 13 TeV", *JHEP* **08** (2020) 139, `doi:10.1007/JHEP08(2020)139`, `arXiv:2005.08694`.

[30] ATLAS Collaboration, "Search for Higgs boson decays into a pair of light bosons in the $bb\mu\mu$ final state in pp collision at $\sqrt{s} =$ 13 TeV with the ATLAS detector", *Phys. Lett. B* **790** (2019) 1, `doi:10.1016/j.physletb.2018.10.073`, `arXiv:1807.00539`.

[31] CMS Collaboration, "Search for exotic decays of the Higgs boson to a pair of pseudoscalars in the $\mu\mu$bb and $\tau\tau$bb final states", *Eur. Phys. J. C* **84** (2024) 493, `doi:10.1140/epjc/s10052-024-12727-4`, `arXiv:2402.13358`.

[32] ATLAS Collaboration, "Search for Higgs boson decays into pairs of light (pseudo)scalar particles in the $\gamma\gamma jj$ final state in pp collisions at $\sqrt{s} =$ 13 TeV with the ATLAS detector", *Phys. Lett. B* **782** (2018) 750, `doi:10.1016/j.physletb.2018.06.011`, `arXiv:1803.11145`.

[33] CMS Collaboration, "Search for light pseudoscalar boson pairs produced from decays of the 125 GeV Higgs boson in final states with two muons and two nearby tracks in pp collisions at $\sqrt{s} =$ 13 TeV", *Phys. Lett. B* **800** (2020) 135087, `doi:10.1016/j.physletb.2019.135087`, `arXiv:1907.07235`.

[34] CMS Collaboration, "Search for the decay of the Higgs boson to a pair of light pseudoscalar bosons in the final state with four bottom quarks in proton-proton collisions at $\sqrt{s} =$ 13 TeV", *JHEP* **06** (2024) 097, `doi:10.1007/JHEP06(2024)097`, `arXiv:2403.10341`.

[35] CMS Collaboration, "Search for the exotic decay of the Higgs boson into two light pseudoscalars with four photons in the final state in proton-proton collisions at $\sqrt{s} =$ 13 TeV", *JHEP* **07** (2023) 148, `doi:10.1007/JHEP07(2023)148`, `arXiv:2208.01469`.

[36] CMS Collaboration, "Search for exotic Higgs boson decays $H \to \mathcal{A}\mathcal{A} \to 4\gamma$ with events containing two merged diphotons in proton-proton collisions at $\sqrt{s} =$ 13 TeV", *Phys. Rev. Lett.* **131** (2023) 101801, `doi:10.1103/PhysRevLett.131.101801`, `arXiv:2209.06197`.

[37] CMS Collaboration, "The CMS experiment at the CERN LHC", *JINST* **3** (2008) S08004, `doi:10.1088/1748-0221/3/08/S08004`.

[38] CMS Collaboration, "Development of the CMS detector for the CERN LHC Run 3", *JINST* **19** (2024) P05064, `doi:10.1088/1748-0221/19/05/P05064`.

[39] CMS Collaboration, "Performance of the CMS Level-1 trigger in proton-proton collisions at $\sqrt{s} =$ 13 TeV", *JINST* **15** (2020) P10017, `doi:10.1088/1748-0221/15/10/P10017`, `arXiv:2006.10165`.

[40] CMS Collaboration, "The CMS trigger system", *JINST* **12** (2017) P01020, `doi:10.1088/1748-0221/12/01/P01020`, `arXiv:1609.02366`.

[41] T. Sjöstrand et al., "An introduction to PYTHIA 8.2", *Comput. Phys. Commun.* **191** (2015) 159, `doi:10.1016/j.cpc.2015.01.024`, `arXiv:1410.3012`.

[42] J. Alwall et al., "The automated computation of tree-level and next-to-leading order differential cross sections, and their matching to parton shower simulations", *JHEP* **07** (2014) 079, `doi:10.1007/JHEP07(2014)079`, `arXiv:1405.0301`.

[43] G. Bozzi, S. Catani, D. de Florian, and M. Grazzini, "Transverse-momentum resummation and the spectrum of the Higgs boson at the LHC", *Nucl. Phys. B* **737** (2006) 73, `doi:10.1016/j.nuclphysb.2005.12.022`, `arXiv:hep-ph/0508068`.

[44] D. de Florian, G. Ferrera, M. Grazzini, and D. Tommasini, "Transverse-momentum resummation: Higgs boson production at the Tevatron and the LHC", *JHEP* **11** (2011) 064, `doi:10.1007/JHEP11(2011)064`, `arXiv:1109.2109`.

[45] NNPDF Collaboration, "Parton distributions from high-precision collider data", *Eur. Phys. J. C* **77** (2017) 663, `doi:10.1140/epjc/s10052-017-5199-5`, `arXiv:1706.00428`.

[46] S. Alioli, P. Nason, C. Oleari, and E. Re, "NLO Higgs boson production via gluon fusion matched with shower in POWHEG", *JHEP* **04** (2009) 002, `doi:10.1088/1126-6708/2009/04/002`, `arXiv:0812.0578`.

[47] P. Nason, "A New method for combining NLO QCD with shower Monte Carlo algorithms", *JHEP* **11** (2004) 040, `doi:10.1088/1126-6708/2004/11/040`, `arXiv:hep-ph/0409146`.

[48] S. Frixione, P. Nason, and C. Oleari, "Matching NLO QCD computations with Parton Shower simulations: the POWHEG method", *JHEP* **11** (2007) 070, `doi:10.1088/1126-6708/2007/11/070`, `arXiv:0709.2092`.

[49] CMS Collaboration, "Extraction and validation of a new set of CMS PYTHIA8 tunes from underlying-event measurements", *Eur. Phys. J. C* **80** (2020) 4, `doi:10.1140/epjc/s10052-019-7499-4`, `arXiv:1903.12179`.

[50] J. Alwall et al., "Comparative study of various algorithms for the merging of parton showers and matrix elements in hadronic collisions", *Eur. Phys. J. C* **53** (2008) 473, `doi:10.1140/epjc/s10052-007-0490-5`, `arXiv:0706.2569`.

[51] GEANT4 Collaboration, "GEANT4–a simulation toolkit", *Nucl. Instrum. Meth. A* **506** (2003) 250, `doi:10.1016/S0168-9002(03)01368-8`.

[52] J. Allison et al., "Geant4 developments and applications", *IEEE Trans. Nucl. Sci.* **53** (2006) 270, `doi:10.1109/TNS.2006.869826`.

[53] CMS Collaboration, "Particle-flow reconstruction and global event description with the CMS detector", *JINST* **12** (2017) P10003, `doi:10.1088/1748-0221/12/10/P10003`, `arXiv:1706.04965`.

[54] CMS Collaboration, "Description and performance of track and primary-vertex reconstruction with the CMS tracker", *JINST* **9** (2014) P10009, `doi:10.1088/1748-0221/9/10/P10009`, `arXiv:1405.6569`.

[55] CMS Collaboration, "Technical proposal for the Phase-II upgrade of the Compact Muon Solenoid", CMS Technical Proposal CERN-LHCC-2015-010, CMS-TDR-15-02, 2015.

[56] CMS Collaboration, "Performance of the CMS muon detector and muon reconstruction with proton-proton collisions at $\sqrt{s} = 13$ TeV", *JINST* **13** (2018) P06015, doi:10.1088/1748-0221/13/06/P06015, arXiv:1804.04528.

[57] M. Cacciari, G. P. Salam, and G. Soyez, "The anti-k_T jet clustering algorithm", *JHEP* **04** (2008) 063, doi:10.1088/1126-6708/2008/04/063, arXiv:0802.1189.

[58] M. Cacciari, G. P. Salam, and G. Soyez, "FastJet user manual", *Eur. Phys. J. C* **72** (2012) 1896, doi:10.1140/epjc/s10052-012-1896-2, arXiv:1111.6097.

[59] CMS Collaboration, "Jet energy scale and resolution in the CMS experiment in pp collisions at 8 TeV", *JINST* **12** (2017) P02014, doi:10.1088/1748-0221/12/02/P02014, arXiv:1607.03663.

[60] E. Bols et al., "Jet Flavour Classification Using DeepJet", *JINST* **15** (2020) P12012, doi:10.1088/1748-0221/15/12/P12012, arXiv:2008.10519.

[61] CMS Collaboration, "Performance summary of AK4 jet b tagging with data from proton-proton collisions at 13 TeV with the CMS detector", CMS Detector Performance Summary CMS-DP-2023-005, 2023.

[62] CMS Collaboration, "Identification of heavy-flavour jets with the CMS detector in pp collisions at 13 TeV", *JINST* **13** (2018) P05011, doi:10.1088/1748-0221/13/05/P05011, arXiv:1712.07158.

[63] LHC Higgs Cross Section Working Group Collaboration, D. de Florian et al., "Handbook of LHC Higgs Cross Sections: 4. Deciphering the Nature of the Higgs Sector", 10, 2016. doi:10.23731/CYRM-2017-002.

[64] M. Lisanti and J. G. Wacker, "Discovering the Higgs boson with low mass muon pairs", *Phys. Rev. D* **79** (2010) 115006, doi:10.1103/PhysRevD.79.115006, arXiv:0903.1377.

[65] R. J. Barlow and C. Beeston, "Fitting using finite Monte Carlo samples", *Comput. Phys. Commun.* **77** (1993) 219, doi:10.1016/0010-4655(93)90005-W.

[66] CMS Collaboration, "Precision luminosity measurement in proton-proton collisions at $\sqrt{s} = 13$ TeV in 2015 and 2016 at CMS", *Eur. Phys. J. C* **81** (2021) 800, doi:10.1140/epjc/s10052-021-09538-2, arXiv:2104.01927.

[67] CMS Collaboration, "CMS luminosity measurement for the 2017 data-taking period at $\sqrt{s} = 13$ TeV", CMS Physics Analysis Summary CMS-PAS-LUM-17-004, 2018.

[68] CMS Collaboration, "CMS luminosity measurement for the 2018 data-taking period at $\sqrt{s} = 13$ TeV", CMS Physics Analysis Summary CMS-PAS-LUM-18-002, 2019.

[69] CMS Collaboration, "Measurement of the inclusive W and Z production cross sections in pp collisions at $\sqrt{s} = 7$ TeV", *JHEP* **10** (2011) 132, doi:10.1007/JHEP10(2011)132, arXiv:1107.4789.

[70] NNPDF Collaboration, "Parton distributions for the LHC Run II", *JHEP* **04** (2015) 040, doi:10.1007/JHEP04(2015)040, arXiv:1410.8849.

[71] J. Pumplin et al., "New generation of parton distributions with uncertainties from global QCD analysis", *JHEP* **07** (2002) 012, doi:10.1088/1126-6708/2002/07/012, arXiv:hep-ph/0201195.

[72] CMS Collaboration, "The CMS statistical analysis and combination tool: COMBINE", 2024. `arXiv:2404.06614`. Submitted to *Comput. Softw. Big Sci.*

[73] W. Verkerke and D. P. Kirkby, "The RooFit toolkit for data modeling", *eConf* **C0303241** (2003) MOLT007, `arXiv:physics/0306116`.

[74] L. Moneta et al., "The RooStats Project", *PoS* **ACAT2010** (2010) 057, `doi:10.22323/1.093.0057`, `arXiv:1009.1003`.

[75] U. Haisch, J. F. Kamenik, A. Malinauskas, and M. Spira, "Collider constraints on light pseudoscalars", *JHEP* **03** (2018) 178, `doi:10.1007/JHEP03(2018)178`, `arXiv:1802.02156`.

[76] M. Baumgart and A. Katz, "Implications of a new light scalar near the bottomonium regime", *JHEP* **08** (2012) 133, `doi:10.1007/JHEP08(2012)133`, `arXiv:1204.6032`.